Finite Elements in Analysis and Design 240 (2024) 104212

Contents lists available at ScienceDirect

Finite Elements in Analysis & Design

journal homepage: www.elsevier.com/locate/finel

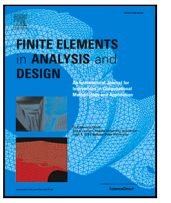

Numerical dispersion and dissipation in 3D wave propagation for polycrystalline homogenization

Feihong Liu [a], Andrea P. Argüelles [a], Christian Peco [a,b,*]

[a] Department of Engineering Science and Mechanics, The Pennsylvania State University, University Park, State College, PA, 16802, USA
[b] Institute for Computational and Data Sciences, Pennsylvania State University, University Park, State College, PA, 16802, USA

ARTICLE INFO

Keywords:
Wave equations
Finite element analysis
Representative volume element
Frequency-domain analysis
Time–history analysis

ABSTRACT

The engineering design of metamaterials with selected acoustic properties necessitates adequate prediction of the elastic wave propagation across various domains and specific frequency ranges. This study proposes a systematic approach centered on the finite element characterization of the three-dimensional Green's function for a representative volume element. The inherent characteristics of broadband waves and singular impulses contribute to notable challenges related to accuracy and high-frequency oscillations, and thus the emphasis is set on providing an exhaustive analysis for this numerical characterization scheme. The study focuses on the broadband wave dispersion and requisite considerations for numerical damping, and evaluates the impact of dissipation and space–time discretization schemes for optimal performance. In contrast to conventional methods that employ a plane wave, the proposed approach does not need extra assumptions on the enforcement of boundary conditions and can effectively consider the influences of length scale from the material configurations. A quasi-equiaxed polycrystalline ice microstructure is utilized as an application example for homogenizing heterogeneous materials, in line with advancements in cryo-ultrasonic testing techniques.

1. Introduction

The ultrasonic testing approach is among the most widely used non-destructive testing techniques [1]. As waves propagate through the tested medium, the transmitted energy reveals variations due to porosity, cracks, or impurities, which can be used to determine the potential damage. To evaluate these differences, prior knowledge of the fundamental acoustic properties of a pure or undamaged medium is often essential, especially within the ultrasonic frequency range across various scales [2]. However, many continuum media, regardless of gas, liquid, or solid, are intrinsically heterogeneous. This heterogeneity can lead to distinct elastic wave scattering and absorption mechanisms, especially when complex microstructures or mechanical conditions exist. Consequently, on the macroscopic level, this results in diverse homogenized acoustic properties. An important form of this heterogeneity is associated with the configurations of material, such as polycrystalline microstructures as shown in Fig. 1 or different material phase distributions [3]. Additionally, factors like residual stress [4], micro-damage [5], or bonding conditions [6] can also influence the determination of acoustic parameters.

The acoustic property measurements can exhibit a correlation with microstructural characteristics. Over the past few decades, the experimental measurement area has witnessed increasing interest, especially with advancements in ultrasonic testing methodologies [8]. The accuracy of these measurements can be compromised by various factors [9], such as coupling and surface conditions.

* Corresponding author at: Department of Engineering Science and Mechanics, The Pennsylvania State University, University Park, State College, PA, 16802, USA.
E-mail address: christian.peco@psu.edu (C. Peco).

https://doi.org/10.1016/j.finel.2024.104212
Received 3 March 2024; Received in revised form 7 June 2024; Accepted 5 July 2024
Available online 18 July 2024

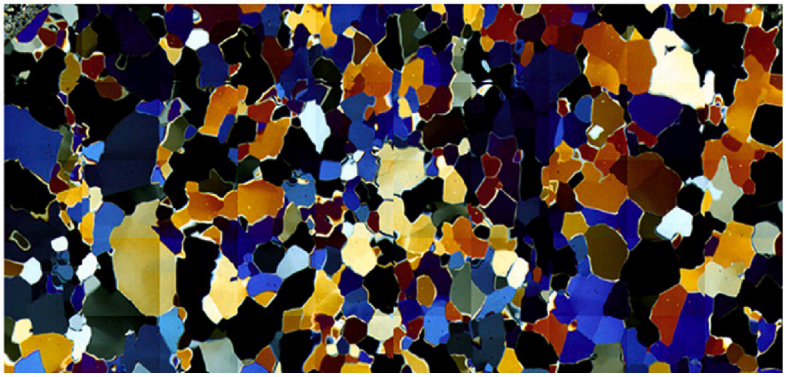

Fig. 1. The polycrystalline microstructures of natural ice thin film [7]. Each crystal shows a different color due to the birefringence.

This often necessitates sample preprocessing, which can be both time-consuming and costly for certain materials. As a result, analytical or numerical predictions become attractive, especially for studies that demand a parametric analysis of configuration or material properties. The (semi-)analytical or numerical prediction of homogenized wave behavior over the heterogeneous medium usually requires certain assumptions. A straightforward approach is to directly approximate the displacement field over the medium, which results in averaging the stiffness tensor. The calculation of the average elastic constants of material properties will then lead to a quasi-static prediction in the Rayleigh region [10]. Common quasi-static approaches include Voigt [11], Reuss [12], Hill average [13], self-consistent method [14], and asymptotic expansion method [15]. Vel et al. [16] provide synthetic numerical comparisons in quasi-static homogenization for the polycrystalline structures.

The propagation of waves through heterogeneous media often involves scattering behaviors or absorptions due to intrinsic microstructures and variations in material properties. In many cases, such as polycrystalline media, scattering predominantly influences the homogenization of acoustic parameters [17]. When considering larger scales where multiple scatterings occur, wave propagation can be described as a stochastic process, necessitating an evaluation of mean responses. Keller et al. [18] introduced a stochastic operator theory for slightly heterogeneous media, known as the Keller approximation. This approach has been applied by Stanke and Kino [10] to non-textured and equiaxed materials with minor single-crystal anisotropy. Weaver [19] further advanced homogenization methodologies, formulating them through statistical physics based on the Dyson equation and the first-order smoothing approximation (FOSA). FOSA is recognized as a specific instance of the Born expansion ensemble, utilizing the second-order moment [20–22], and is deemed equivalent to the second-order Keller approximation [23]. In Weaver's work [19], the covariance function is bifurcated into a tensorial term, determined by material properties, and a dependence term, expressed through the statistical description. This statistical description is typically characterized by an inverse exponential function $\eta(r) = \exp(-r/l)$, with l representing the micro-scale correlation length associated with crystallite size.

However, such assumptions in analytical and semi-analytical approaches have sometimes shown inconsistencies with experimental data. Two strategies have been put forward to reconcile these discrepancies. On the one hand, many studies have proposed to modify the analytical representation of the spatial term. Argüelles and Turner [17] suggested employing a log-normal distribution function for the micro-scale length, characterizing grain size by its deviation. This concept was empirically evaluated by Bai et al. [24] for α-titanium alloys. Saju et al. [25] investigated the impact on nonlinearity resulting from grain size distribution in one-dimensional microstructures. Liu et al. [26] proposed retaining the exponential form but empirically calculating the correlation length as opposed to employing a mean grain size. Recently, Argüelles [27] proposed employing a Von Kármán form of the correlation function in order to incorporate additional microstructural characteristics. On the other hand, numerical tools, such as the Finite Element Method (FEM), have become pivotal in modeling wave propagation through materials with complex microstructures or diverse material constituents. Typically, this modeling is implemented on a representative volume element (RVE) that captures the morphology and spatial distribution of material properties [28,29]. The randomness inherent in these models is governed by random variables or probability distribution functions, which can differ from one scenario to another [30–32]. A significant advantage of this approach is its independence from the statistical properties of materials and microstructures, often allowing for more accurate capture of microscale behaviors [33]. This capability is crucial in understanding the influence of scale length on homogenized material properties. Numerous studies have successfully applied FEM with time integration for solving elastodynamic equations and characterizing material properties [2,34–37]. In recent years, Tie et al. [38–40] have highlighted the potential of Discontinuous Galerkin methods in wave modeling.

Despite these advances, one of the main challenges in the field is that most of these studies model plane waves within a narrow-band frequency by applying ideal boundary conditions to ensure irrotational or divergence-free displacement patterns of plane waves to facilitate the determination of macroscopic longitudinal or transverse properties. Periodic boundary conditions are also commonly employed to mitigate reflection effects and reduce measurement errors [34]. However, these approaches often lead to under-discussed and intricate accuracy issues in determining acoustic parameters. For example, the enforcement of symmetric boundary conditions requires the material to exhibit statistical isotropy at the macro-scale. Failing this, the isotropic Helmholtz

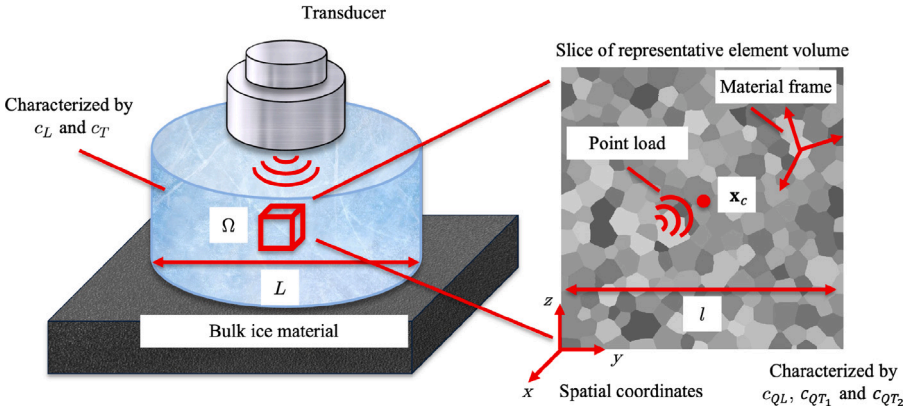

Fig. 2. Sketch of statistically isotropic ice material and its RVE (c_L: longitudinal speed, c_T: transverse speed, c_{QL}: quasi-longitudinal speed, c_{QT_1} and c_{QT_2}: quasi-transverse speeds).

decomposition cannot be accurately achieved [41]. This limitation also hinders the characterization of general material properties, particularly in textured materials known for specific statistical anisotropy [23].

Instead, here we focus on spherical wave propagation and broad-band frequency waves which, though proven effective in many fields, are seldom employed in the numerical characterization of ultrasonic parameters. A notable application of these waves is the elastic Green's function (or Green's dyadic), where a point-source response is equated to Green's function convolved with a wavelet. Since the pioneering work by Weaver et al. [19,42], there have been significant contributions from researchers like Campillo et al. [43] and Wapenaar et al. [44–46], emphasizing the utility of acoustic Green's function. This approach has been instrumental in exploring physical fields around structures at both microscopic [47–49] and macroscopic scales, particularly in seismology [45,46]. Modeling broad-band frequency waves, however, presents challenges such as numerical dispersion and spurious oscillations, necessitating additional solutions. Extensive studies have discussed these challenges, proposing various modifications and treatments to mitigate numerical dispersion in elastic wave problems [50–56]. In this work, we leverage FEM to develop a spherical Green's function-based RVE approach for characterizing elastic waves in complex heterogeneous media.

The subsequent sections are organized as follows. Section 2 introduces the methodology and implementation scheme, including the problem statement, generation of microstructures, and characterization scheme in using the FEM with time integration for the wave modeling study. To establish this framework, we believe that an error analysis of the wave error resulting from numerical discretization is necessary. Section 3 provides error analysis where we emphasize the impact of numerical dispersion, and damping in characterizing frequency domain solutions. In Section 4, we test this characterization scheme with both homogeneous benchmark and heterogeneous medium in 3D space. The quasi-equiaxed polycrystalline microstructures that show statistical isotropy are emphasized and taken as a paradigm in showing the general homogenization of heterogeneous medium and the characterization process in determining the acoustic properties. Finally, Section 5 presents the conclusions and future work.

2. FEM-RVE Green's function approach: formulation and implementation

This section introduces our proposed homogenization procedure. This procedure is based on the computational evaluation and postprocessing of assumption-reduced Green's functions over the microstructure RVEs. In particular, note that we calculate and characterize Green's function beyond the conventional approaches, which use plane waves and enforce specific boundary conditions to achieve macroscopically divergence-free or irrotational displacement fields. A typical ice specimen target and its corresponding RVE are depicted in Fig. 2. The bulk material, with macro-scale dimension L, is characterized as statistically isotropic and manifests longitudinal and transverse waves, as shown in Fig. 2 (left). On a finer scale, an RVE will be used to initiate our proposed homogenization procedure to capture the average material's behavior from the smaller length scale (polycrystalline microstructures on the right of Fig. 2). The Green's function of an elastodynamic problem is equivalent to solving an initial value problem (IVP) excited by the point load at $\mathbf{x}_c$ as shown in Fig. 2 (right). FEM with a specific time integration scheme is then used for stepping this IVP. The Green's function results over this RVE domain are utilized to determine homogenized properties over frequency ω, such as the averaged longitudinal wave speed $\bar{c}_L(\omega)$.

This methodology offers further advantages by eliminating boundary reflection errors in homogenization and facilitating scale effect discussions without necessitating special assumptions on the displacement field. Furthermore, it is critical to accurately describe an RVE that adequately represents the material. In Section 2.1, we elaborate on the modeling scheme for polycrystalline structures aimed at achieving a quasi-equiaxed morphology. The IVP problem and its FEM implementation are described in Section 2.2. Finally, Section 2.3 discusses a characterization scheme based on the space–time and transformed space-frequency solutions, from which the homogenized properties are derived. Fig. 3 summarizes the key implementation procedures for the proposed FEM-RVE Green's function homogenization procedure. It should be noted that the final homogenized properties can be essentially different as the statistically fitted model is changed. In the case of textured or statistically anisotropic materials, for

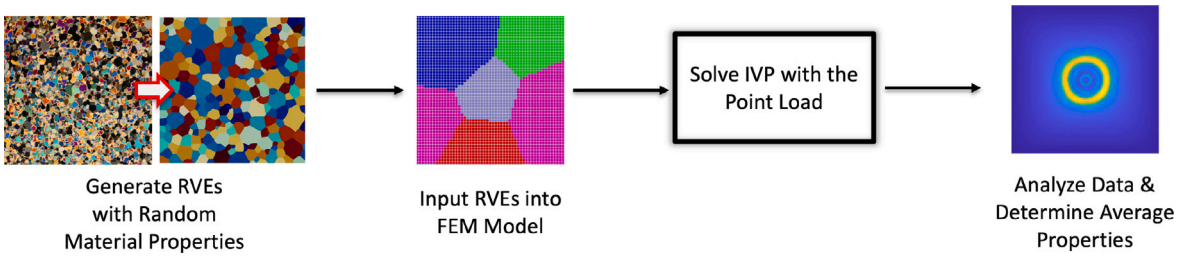

Fig. 3. The implementation procedures of Green's function RVE approach.

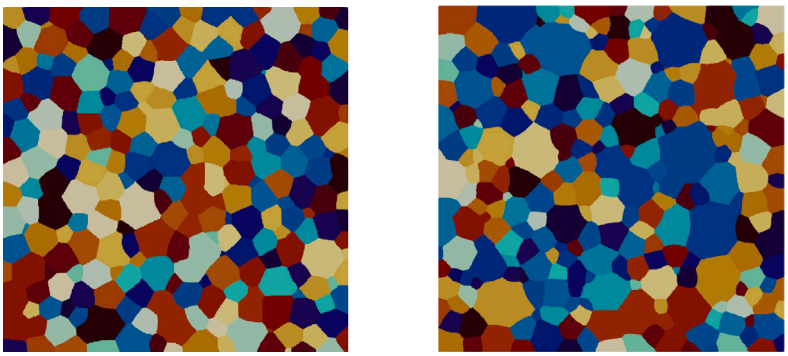

(a) Deviation = 0.2. (b) Deviation = 0.4.

Fig. 4. The influence from the deviation in ESD probability density function to the polycrystal morphology: (a) Deviation = 0.2; (b) Deviation = 0.4.

example, the homogenization may place varying emphasis on certain directions. Further exploration of this aspect will be addressed in future studies.

2.1. Numerical modeling the RVE: polycrystalline microstructures

Polycrystalline materials consist of a large number of grains with randomly distributed crystallographic orientations and are separated by grain boundaries. Under the Cartesian coordinates, the elasticity tensor under the laboratory axes C_{ijkl} can be calculated through the orthogonal transformations by

$$C_{ijkl} = \sum_{\alpha,\beta,\gamma,\delta=1}^{3} a_{i\alpha}a_{j\beta}a_{k\gamma}a_{l\delta}C'_{\alpha\beta\gamma\delta}, \tag{1}$$

where C'_{ijkl} is the elasticity tensor under the material (crystalline) axes and $\mathbf{a}(\zeta_1, \zeta_2, \zeta_3)$ are rotation matrices defined by the Euler angles $(\zeta_1, \zeta_2, \zeta_3)$ representing the transformation between the crystalline axes and the laboratory axes. The morphological properties of polycrystalline microstructures can be influenced by a variety of factors, including thermodynamics and material chemistry. This study considers that the geometry of such microstructures can be replicated by partitioning the RVE into a series of compact cells assembled. Consequently, weak bond behavior at grain boundaries will not be discussed herein. The generation of these polycrystalline structures is facilitated by *Neper* [57], an open-source software package for polycrystal generation based on Laguerre tessellation.

The morphology is characterized by the distributions of two key indicators: *equivalent spherical diameter* (ESD) and *sphericity*. Lognormal distributions are used for both indicators. The equivalent spherical diameter represents the characteristic size, where the mean reflects the average size and the deviation indicates the size variation. Fig. 4 displays the sliced RVE profile at varying levels of deviation. Notably, a smaller deviation results in a more uniform grain size distribution, as illustrated in Fig. 4(a). Sphericity reflects how much the shape of a discretized grain deviates from a spherical shape, calculated as the ratio of the grain's surface area to that of an equivalent sphere. The standard deviation for ESD is set at 0.06 and the sphericity distribution has an average of 0.86 and a standard deviation of 0.03 to mimic the quasi-equiaxed feature of ice. We suggest the generated geometry be discretized by using the equidistant structured mesh. A distinguished advantage of this meshing scheme is that it can alleviate the artificial scattering due to the difference brought by element stiffness. The refinement of the boundary tessellation is an important numerical parameter and is extensively discussed in Section 4.3.

2.2. Wave equation and FEM discretization

To characterize the acoustic properties, we propose calculating Green's function for the specific RVE under the infinite domain assumption. Considering the wave is not subjected to boundary conditions and lets the excitation occur at $t = 0$, the strong form for solving Green's function of elastodynamic problem can be expressed as follows

$$\begin{aligned} &-\rho u_{i,tt} + \sigma_{ij,j} = f_i, \text{ in } \Omega\times]0,T[\\ &u_i(\mathbf{x},0) = u_{0i}(\mathbf{x}),\ \mathbf{x}\in\Omega \\ &u_{i,t}(\mathbf{x},0) = \dot{u}_{0i}(\mathbf{x}),\ \mathbf{x}\in\Omega \end{aligned} \quad , \tag{2}$$

where ρ, $u_i(\mathbf{x})$, σ_{ij}, f_i, u_{0i}, and $\dot{u}_{0i}$ represent the density, displacement, Cauchy stress, unit force impulse, initial displacement, and initial velocity, respectively. For Green's dyadic $G_{im}(t,\mathbf{x},\mathbf{x}')$, the subscript i denotes the component of displacement $\mathbf{u}$ and the force term is written by

$$f_i(t,\mathbf{x}-\mathbf{x}_c) = \delta_{im}\delta(\mathbf{x}-\mathbf{x}_c)\delta(t), \tag{3}$$

where δ_{im}, $\delta(\cdot)$ and $\mathbf{x}_c$ are Kronecker-delta, Dirac-delta function, and the position of impulse. m denotes the non-zero component of the unit impulse. We always set the impulse position $\mathbf{x}_c$ to be the center of an RVE (Ω) to save the computational cost in each test. To obtain the weak form for FEM, we employ the integrable interpolation function to approximate this singular unit point load. For a discretized node $\mathbf{x}_i \in \Omega'$ where $\Omega' \subset \Omega$, the FEM shape functions $N_{\mathbf{x}_i}(\mathbf{x})$ are particularly well-suited to approximate the spatial unit impulse from $\delta(\mathbf{x}_i - \mathbf{x}_c)$ due to the Kronecker-Delta property, defined as

$$N_{\mathbf{x}_c}(\mathbf{x}_i) = \begin{cases} 1 & i = c \\ 0 & i \neq c. \end{cases} \tag{4}$$

An example FEM shape function using the 8-node hexahedron element under the natural coordinate can be written as follows:

$$N_i(x,y,z) = N_{\mathbf{x}_i}(x,y,z) = \frac{1}{8}(1+x_i x)(1+y_i y)(1+z_i z),\ i = 1,\ 2,\ \cdots, 8. \tag{5}$$

where $x_i,\ y_i,\ z_i = -1$ or 1 are the natural coordinates of the eight vertices. This study employed the 8-node hexahedron element for all following numerical tests for adequate accuracy and computational cost.

On the time domain, a C^0 interpolation is considered using the time integration. A fixed time step scheme where time interval Δt is constant is utilized in this paper, the temporal unit delta function from $\delta(t)$ can be expressed by a step function $H(t)$

$$H(t) = \begin{cases} \frac{1}{\Delta t} & 0 \le t < \Delta t \\ 0 & t \ge \Delta t. \end{cases} \tag{6}$$

In this way, we obtained the approximated unit force impulse by

$$f_i(t,\mathbf{x}-\mathbf{x}_c) \approx \delta_{im} N_{\mathbf{x}}(\mathbf{x}_c) H(t). \tag{7}$$

Consider the zero initial conditions where $u_{0i}(\mathbf{x}) = 0$ and $\dot{u}_{0i}(\mathbf{x}) = 0$ for $\mathbf{x} \in \Omega$. The corresponding weak formulation of the elastodynamic problem for FEM can then be constructed, which is to find $\mathbf{u}(t) \in \mathcal{H}^1$, $t \in [0,T]$, such that for all $\mathbf{w} \in \mathcal{H}^1$

$$\int_\Omega \rho w_i \ddot{u}_i d\Omega + \int_\Omega w_{(i,j)} C_{ijkl} u_{(k,l)} d\Omega = \int_\Omega w_i f_i d\Omega\ , \tag{8}$$

where $(\cdot)_{(i,j)} = \frac{(\cdot)_{i,j}+(\cdot)_{j,i}}{2}$ and therefore $u_{(i,j)}$ is the infinitesimal strain tensor (i.e., ϵ_{ij}). Under the linear elastodynamic case, the Cauchy stress tensor can be defined by the generalized Hooke's law $\sigma_{ij} = C_{ijkl}\epsilon_{kl}$. The FE approximation leads to the approximated displacement field $u_i^h \in \mathcal{V},\ \mathcal{V} \subset \mathcal{H}^1$ which is given by

$$u_i^h(\mathbf{x},t) = \Sigma_{j=1}^{nn} N_{\mathbf{x}_j}(\mathbf{x}) d_i(\mathbf{x}_j,t), \tag{9}$$

where nn denotes the number of nodes connected with $\mathbf{x}$ and $\mathbf{d}(\mathbf{x},t)$ is the nodal displacement. As the Bubnov–Galerkin scheme is considered, the approximated $w_i^h \in \mathcal{V}$ using the same interpolation scheme as u_i^h. Thus, the weak formulation of the elastodynamic equation (Eq. (2)) can be written in the matrix form

$$\mathbf{M}\ddot{\mathbf{d}}^{(n+1)} + \mathbf{K}\mathbf{d}^{(n+1)} = \mathbf{F}^{(n+1)}, \tag{10}$$

where $\mathbf{M}$, $\mathbf{K}$, $\mathbf{F}$, $\ddot{\mathbf{d}}^{(n)}$, and $\mathbf{d}^{(n)}$ are global mass matrix, stiffness matrix, force vector, acceleration vector, and displacement vector, respectively. The superscript n denotes the current time step. The assembling of the global matrix (vector) can be expressed by

$$\mathbf{M} = \Sigma_{e=1}^{ne}(\mathbf{m}^e),\ \mathbf{m}^e = [m_{pq}^e],\ m_{pq}^e = \delta_{ij}\int_{\Omega_e} \rho N_a N_b d\Omega, \tag{11}$$

$$\mathbf{K} = \Sigma_{e=1}^{ne}(\mathbf{k}^e),\ \mathbf{k}^e = [k_{pq}^e],\ k_{pq}^e = \mathbf{e}_i^T \int_{\Omega_e} \mathbf{B}_a^T \mathbf{D}\mathbf{B}_b d\Omega \mathbf{e}_j, \tag{12}$$

$$\mathbf{F} = \Sigma_{e=1}^{ne}(\mathbf{f}^e),\ \mathbf{f}^e = [f_p^e],\ f_p^e = \int_{\Omega_e} N_a f_i d\Omega, \tag{13}$$

where ne denotes the total number of elements. $\mathbf{e}_i$ is the basis vector. $\mathbf{D}$ is the elasticity matrix under Voigt notation. $\mathbf{B}$ is called the strain matrix with the form

$$\mathbf{B}_i = \begin{bmatrix} N_{i,1} & 0 & 0 \\ 0 & N_{i,2} & 0 \\ 0 & 0 & N_{i,3} \\ 0 & N_{i,3} & N_{i,2} \\ N_{i,3} & 0 & N_{i,1} \\ N_{i,2} & N_{i,1} & 0 \end{bmatrix}, \tag{14}$$

The α-method [58] is used for stepping the temporal solutions and following analysis in this paper, which is given by

$$\mathbf{M}\ddot{\mathbf{d}}^{(n+1)} + (1+\alpha)\mathbf{K}\mathbf{d}^{(n+1)} - \alpha\mathbf{K}\mathbf{d}^{(n)} = \mathbf{F}_{n+\alpha}, \tag{15a}$$

$$\mathbf{d}^{(n+1)} = \mathbf{d}^{(n)} + \Delta t\dot{\mathbf{d}}^{(n)} + \Delta t^2[(\frac{1}{2} - \beta)\ddot{\mathbf{d}}^{(n)} + \beta\ddot{\mathbf{d}}^{(n+1)}], \tag{15b}$$

$$\dot{\mathbf{d}}^{(n+1)} = \dot{\mathbf{d}}^{(n)} + \Delta t[(1-\gamma)\ddot{\mathbf{d}}^{(n)} + \gamma\ddot{\mathbf{d}}^{(n+1)}], \tag{15c}$$

where $\dot{\mathbf{d}}^{(n)}$ is the velocity vector. α, β, γ are time integration parameters of α-method.

2.3. Green's function characterization scheme

After the generated RVE is employed for the elastodynamic problem stated in Section 2.2, the calculated Green's function can then be processed by the characterization scheme for homogenization. Because of the heterogeneity, Green's function $G_{im}(t, \mathbf{x}, \mathbf{x}_c)$ is a multi-variable function, dependent on a receiver at point $\mathbf{x}$ and an impulse source at $\mathbf{x}_c$. The homogenization then aims to find an average Green's function expressed by the relative position or radial vector $\mathbf{r} = \mathbf{x} - \mathbf{x}_c = r\hat{\mathbf{r}}$ where $r = |\mathbf{r}|$ represents the propagation distance, and $\hat{\mathbf{r}}$ is the propagation direction vector.

In textured materials where material properties exhibit a specific preferred orientation, Green's function becomes a general function of $\mathbf{r}$. However, for statistically isotropic materials, such as ice polycrystals, their acoustic properties can be defined by a distance function solely dependent on r. In this case, the measurement of space–time speed can then be obtained by tracking the two peak responses of each RVE in the time history [59]. For each receiver $\mathbf{x}$, and their respective peak arrival times t_L (longitudinal) and t_T (transverse), we search the arithmetic average

$$\bar{c}_i = \frac{1}{n}\sum_j^n \frac{r}{t_i(\mathbf{x}_j)}, \mathbf{x}_j \in \Omega, \ (i = L, T), \tag{16}$$

where $\bar{c}_i$ denotes the homogenized longitudinal or transverse wave speeds by averaging all n discretized nodes. By using the Fourier transform (FT) for the calculated space–time Green's function, we will obtain a two-point form of Green's dyadic in the frequency domain by

$$G_{im}(\omega, \mathbf{x}, \mathbf{x}_c) = F_t(G_{im}(t, \mathbf{x}, \mathbf{x}_c)), \tag{17}$$

where $F_t(\cdot) = \frac{1}{2\pi}\int(\cdot)\exp(j\omega t)dt$ denotes the operation of Fourier transform. With the spatial FT, we will be able to further express Green's dyadic in p-space or spatial frequency space

$$G_{im}(\mathbf{p}) = F_{\mathbf{x}}(G_{im}(\omega, \mathbf{x}, \mathbf{x}_c)), \tag{18}$$

where $F_{\mathbf{x}}(\cdot) = \frac{1}{(2\pi)^3}\int(\cdot)\exp(j\mathbf{p}\cdot(\mathbf{x}-\mathbf{x}_c))d(\mathbf{x}-\mathbf{x}_c)$ denotes the operation of spatial FT. $\mathbf{p}$ is the wave vector. We denote the modeled real wave number and unit wave vector by p and $\hat{\mathbf{p}}$, respectively. To fit a lossless statistically isotropic medium, recall p-space Green's dyadic $G_{im}(\mathbf{p})$ can be written by

$$G_{im}(\mathbf{p}) = \hat{\mathbf{p}}\hat{\mathbf{p}}g^{oL} + (\mathbf{I} - \hat{\mathbf{p}}\hat{\mathbf{p}})g^{oT}, \tag{19}$$

where the bare longitudinal or transverse oscillator is

$$g^{oi} = [\omega^2 - (c_i p)^2]^{-1}, \ \ i = L, \ T. \tag{20}$$

Because the spatial spectrum will present the two major components at $p_i \ \ (i = L, \ T)$. The phase speed comes with

$$c_i(\omega, \hat{\mathbf{p}}) = \omega / p_i(\hat{\mathbf{p}}), \ \ i = L, \ T, \tag{21}$$

where the measurement determined will depend on the propagation direction indicated by the unit wave vector $\hat{\mathbf{p}}$. The average is then applied by using

$$\bar{c}_i(\omega) = \frac{1}{n}\sum_j^n \frac{\omega}{p_i(\hat{\mathbf{p}})}, \ i = L, T. \tag{22}$$

To count on the statistics on morphology, the sampled data should be further extended over repeated tests. Thus, the speed $\bar{c}_i$ is further averaged on m randomly generated RVEs where the formulation is ignored herein.

3. Green's function RVE approach: error and analysis

3.1. Grid dispersion analysis

Characterizing acoustic properties demands a higher degree of accuracy on the numerical modeled physical characteristics than measuring amplitude errors [50]. When the domain size greatly exceeds the wavelength, numerical dispersion, also known as wavelength error, can be distinguished and not negligible. This phenomenon leads to the modeled wave speed $c(\omega)$ deviating from the physical wave speed c_0, even in a homogeneous media. To analyze this numerical dispersion error, we part from the scalar wave equation in the continuum, which is presented as follows:

$$\frac{\partial^2 u}{\partial t^2} - c_0^2 \nabla^2 u = 0, \tag{23}$$

where $u = u(\mathbf{x})$ represents the scalar displacement field and c_0 is the physical wave speed. After space discretization, the α-method is used as a time integrator. Under the structured grid or a uniform discretization, it is useful to express the α-method as a linear multi-step (LMS) form. Let us express the equation of motion (EOM) at time steps t_n and t_{n+1}:

$$\begin{aligned} &\mathbf{M}\ddot{\mathbf{d}}^n + (1+\alpha)\mathbf{K}\mathbf{d}^n - \alpha\mathbf{K}\mathbf{d}^{n-1} = \mathbf{0}, \\ &\mathbf{M}\ddot{\mathbf{d}}^{n+1} + (1+\alpha)\mathbf{K}\mathbf{d}^{n+1} - \alpha\mathbf{K}\mathbf{d}^{n} = \mathbf{0}. \end{aligned} \tag{24}$$

Note that the scalar speed c_0 is contained in stiffness matrix $\mathbf{K}$ for the matrix form. With the displacement approximation in Eq. (15b), we obtain

$$\begin{aligned} &\mathbf{M}\ddot{\mathbf{d}}^{(n)} + \mathbf{K}\mathbf{d}^{(n-1)} + (1+\alpha)\mathbf{K}\{\Delta t\dot{\mathbf{d}}^{(n-1)} + \Delta t^2[(\frac{1}{2}-\beta)\ddot{\mathbf{d}}^{(n-1)} + \beta\ddot{\mathbf{d}}^{(n)}]\} = \mathbf{0}. \\ &\mathbf{M}\ddot{\mathbf{d}}^{(n+1)} + \mathbf{K}\mathbf{d}^{(n)} + (1+\alpha)\mathbf{K}\{\Delta t\dot{\mathbf{d}}^{(n)} + \Delta t^2[(\frac{1}{2}-\beta)\ddot{\mathbf{d}}^{(n)} + \beta\ddot{\mathbf{d}}^{(n+1)}]\} = \mathbf{0}. \end{aligned} \tag{25}$$

As the second equation deducts the first equation above, then we get

$$\begin{aligned} &\mathbf{M}(\ddot{\mathbf{d}}^{(n+1)} - \ddot{\mathbf{d}}^{(n)}) + \mathbf{K}(\mathbf{d}^{(n)} - \mathbf{d}^{(n-1)}) + (1+\alpha)\mathbf{K}\{\Delta t(\dot{\mathbf{d}}^{(n)} - \dot{\mathbf{d}}^{(n-1)}) + \\ &\quad \Delta t^2[(\frac{1}{2}-\beta)(\ddot{\mathbf{d}}^{(n)} - \ddot{\mathbf{d}}^{(n-1)}) + \beta(\ddot{\mathbf{d}}^{(n+1)} - \ddot{\mathbf{d}}^{(n)})]\} = \mathbf{0}. \end{aligned} \tag{26}$$

By recalling Eq. (15c), we can substitute both acceleration and velocity difference terms. After some algebra, we will have

$$\begin{aligned} &\mathbf{d}^{(n+1)} + [(\frac{1}{2} + \frac{1}{2}\alpha - 2\beta + \gamma - 3\alpha\beta + \alpha\gamma)\Delta t^2\mathbf{K} - 2\mathbf{M}]\mathbf{d}^{(n)} \\ &+[(\frac{1}{2} + \beta - \gamma + 3\alpha\beta - 2\alpha\gamma)\Delta t^2\mathbf{K} + \mathbf{M}]\mathbf{d}^{(n-1)} + \alpha(-\frac{1}{2} - \beta + \gamma)\Delta t^2\mathbf{K}\mathbf{d}^{(n-2)} = \mathbf{0}. \end{aligned} \tag{27}$$

When $\alpha = 0$, we reproduce the LMS form of Newmark-β scheme, which is given by

$$(\beta\Delta t^2\mathbf{K} + \mathbf{M})\mathbf{d}^{(n+1)} + [(\frac{1}{2} - 2\beta + \gamma)\Delta t^2\mathbf{K} - 2\mathbf{M}]\mathbf{d}^{(n)} + [(\frac{1}{2} + \beta - \gamma)\Delta t^2\mathbf{K} + \mathbf{M}]\mathbf{d}^{(n-1)} = \mathbf{0}, \tag{28}$$

where the equation will be the same as $\gamma = \frac{1}{2}$ shown in [51] . Finally, a general form to implicitly express the LMS scheme for analysis is given by

$$\mathbf{M}\sum_{m}^{m_t} g_m\mathbf{d}^{(m)} + \mathbf{K}\sum_{n}^{n_t} h_n\mathbf{d}^{(n)} = \mathbf{0}, \tag{29}$$

where g_m and h_n are the coefficients for stiffness and mass terms indicated by Eq. (27), and parameters m_t and n_t denote the number of time points used in the time integrator. Note for different time integration schemes, the number of time points in the stencil can be different (i.e., $m_t \neq n_t$).

Now we can introduce Green's function (spherical wave), which can be expanded into plane waves using the spatial Fourier transform. Suppose we have the exact solution for a plane wave that can be expressed by

$$u = U e^{j(\mathbf{p}\cdot\mathbf{x} - \omega n\Delta t)}, \tag{30}$$

where U is the amplitude of the plane wave. Moreover, we can express the displacement shifted by a specific point $\mathbf{x}_0$ and time instance $t = m\Delta t$ such that

$$u^{(n)}(\mathbf{x}) = u^{(n)}(\mathbf{x_0})e^{j\mathbf{p}\cdot(\mathbf{x}-\mathbf{x_0})}, \quad u^{(n)}(\mathbf{x}) = u^{(m)}(\mathbf{x})e^{-j\omega(n-m)\Delta t}. \tag{31}$$

When uniform spatial (or temporal discretization) is used, each component of the position vector $\mathbf{x}$ (or time instance t_n) can be expressed with nodal numbering by $x_i = n\Delta x$ $(i = 1,\ 2,\ 3;\ n = 1, 2, 3, \ldots)$ (or $t_n = n\Delta t$ $(n = 1, 2, 3, \ldots)$. Δx is the nodal spacing. This operation makes it possible to merge Eq. (29) on a certain interior node by using Eq. (31). Let us denote the nth row of $\mathbf{M}$ and $\mathbf{K}$ associated with the arbitrary interior node by $\mathbf{m}^T$ and $\mathbf{k}^T$, respectively. Recall $p = \omega/c(\omega)$, after canceling the aligned global displacement vector, then the modeled wave speed can be obtained by solving

$$\mathbf{m}^T\mathbf{l}\sum_{m}^{m_t} g'_m + \mathbf{k}^T\mathbf{l}\sum_{n}^{n_t} h'_n = 0, \tag{32}$$

Table 1
The time integration schemes to be evaluated (Eqs. (15a)–(15c)).

Schemes	α	β	γ
I	0	0.25	0.5
II	0.1	0.25	0.5
III	0.3	0.25	0.5
IV	0.33	0.44	0.83

where g'_m and h'_n are shifted by aligning the time step, and **l** is the coefficient vector by expressing the numbering of connected nodes.

The particularized wave speed (Eq. (32)) will be our starting point for subsequent analyses on a variety of approximation schemes. In general, Eq. (32) will be subjected to a dispersion error coming from different sources, namely:

1. **Time integration scheme** (g'_m and h'_n). The time integration scheme will affect the form expressed in linear multi-step on the temporal aspect as shown in Eq. (27).

2. **Quadrature rule or element order** (**m** and **k**). When introducing certain special quadrature rules with a specific time integration scheme or high-order element, the dispersion error can be changed [51,52].

3. **Mass discretization** (**m**). For some circumstances, mass discretization may need to be adapted with the time integration scheme for better accuracy [60].

4. **Nodal spacing and time interval** (g'_m, h'_n, **m**, **k** and **l**). For structured mesh, it is easier to get a quantified form for these factors. While the dispersion error will change if non-structured discretization or adaptive time step is considered.

5. **Propagation direction** (**l**). For 2D or 3D acoustic problems, the dispersion error will vary for different propagation directions [53].

6. **Dimensions and physical wave speed** (g'_m, h'_n, **m**, **k** and **l**). The spatial discretization depends on the dimensions of the problem. And the physical wave speed will lead to the stiffness change.

7. **Dissipation** (g'_m and h'_n). The integration schemes will lead to different numerical dissipation associated with frequencies, which will be further discussed in Section 3.2.

The large number of factors that influence numerical dispersion may render the analysis considerably complex. To facilitate the discussion, it is useful to reduce the parameter space determined by Eq. (32). First, as the structured mesh and constant time step are applied, we can consider the temporal–spatial ratio (TSR) of discretization $\frac{\Delta t}{\Delta x}$, which can be multiplied by the physical wave speed c_0, leading to the Courant–Friedrichs–Lewy number (i.e., $CFL = \frac{c_0 \Delta t}{\Delta x}$). In this way, the effect of nodal spacing, time interval, and wave speed can be unified with a single parameter. It should be noted that for vector-field problems if the TSR $\frac{\Delta t}{\Delta x}$ is considered constant, the CFL of each wave component will not be the same.

Moreover, besides the CFL parameter, our analysis considers the impact of the time integration approach through four different schemes. Table 1 lists the four schemes we are going to discuss in the rest of the paper. Scheme I corresponds to the well-known Newmark-beta scheme with average acceleration [60]. Scheme II and III extend Scheme I by incorporating numerical damping in α-method [58]. Scheme IV further introduces the dissipation from β and γ parameters. In this way, the numerical dispersion discussion on the dissipation issue is indirectly investigated. Note that we do not include here the traditional central difference scheme ($\alpha = 0, \beta = 0, \gamma = 0.5$), which becomes a explicit stepping scheme when lumped mass discretization is used. The schemes we present have mass discretization schemes that align with the time-stepping approach for optimal dispersion error [60–62]. Our accuracy tests concluded that the four schemes exhibit greater performance when using consistent mass and outperform the central difference with lumped mass for the stable CFL number.

To further reduce the dimension of parameter space, all these four schemes share the consistent mass scheme, full integration, structured grids, and constant time steps with 3D linear hexahedral elements. This setup allows an explicit form of **m** and **k** where the remaining unknowns in Eq. (32) include wave number, frequency, physical wave speed, and propagation direction. For instance, for a specific CFL of 0.5, if we set $c_0 = 1.0$ and $\Delta x = 1 \times 10^{-5}$, the time step becomes $\Delta t = 1 \times 10^{-5}$. It should be noted that a wide range of Δx and Δt, up to the order of 10^6 can yield the same dispersion result. This is determined by CFL number, not just the single spatial or temporal spacing. When plotting with the normalized wavelength $2\Delta x/\lambda \in [0, 1]$, the λ will be associated with it and spacing Δx. Note the propagation direction can be expressed by polar and azimuthal angles, which are the only parameters left in Eq. (32) eventually. Finally, the numerical dispersion coming from the particularities of the propagation direction is considered from the analysis through a proposed averaging strategy presented in Section 3.1.1. Along with the aforementioned considerations, our analysis in Section 4 explores the optimal parameter landscape focusing on CFL, the time integration schemes, and the dissipation (Section 3.2).

3.1.1. Propagation direction role and averaging strategy

To illustrate the influence of the propagation direction, here we denote the azimuthal angle θ is measured on the xOy plane from the positive x-axis towards the positive y-axis. The polar angle ϕ is measured on the yOz plane from the positive z-axis towards the xOy plane. Fig. 5 exhibits the numerical dispersion of the trapezoidal rule as $CFL = 0.5,\ 0.7$ and 1.0 where $\phi \in [0, \frac{\pi}{2}]$ and $\theta = 0$. A total of 21 polar angles $\phi \in [0, \frac{\pi}{2}]$ are utilized for direction input. The calculation of numerical dispersion by using Eq. (32) starts with $c_0 = 1.0$, $\Delta x = 1 \times 10^{-7}$, and the time step is accordingly scaled by the CFL numbers. As the final dispersion results are independent of the speed or single spatial or temporal spacing, we tested that $\Delta x \in [10^{-10}, 10^{-4}]$ will be able to reproduce the

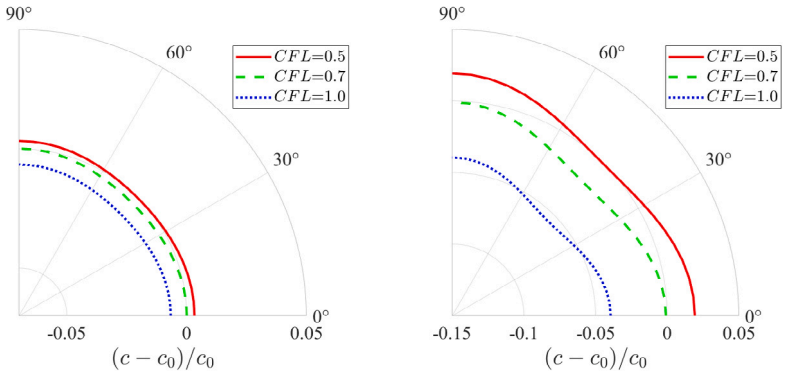

(a) $2\Delta x/\lambda = 0.2$. (b) $2\Delta x/\lambda = 0.5$.

Fig. 5. The numerical dispersion of the trapezoidal scheme (Scheme I in Table 1) associated with ϕ as $\theta = 0$ and: (a) $2\Delta x/\lambda = 0.2$, (b) $2\Delta x/\lambda = 0.5$.

same error curves as $c_0 = 1.0$. From Fig. 5, we can observe the dispersion error of each propagation direction is essentially different for every different CFL number and wavelength. When $2\Delta x/\lambda = 0.2$, the dispersion error is almost the same for each propagation direction. However, at $2\Delta x/\lambda = 0.2$, the dispersion error exhibits directional dependency.

Because the variance of dispersion is associated with propagation direction, we propose to define a mean dispersion error measure through the volumetric average expressed by

$$\left\langle \frac{c-c_0}{c_0} \right\rangle = \frac{1}{4\pi}\int_0^{2\pi}\int_0^{\pi} c(\mathbf{p}(\theta,\phi))sin(\phi)d\phi d\theta - 1, \tag{33}$$

where $\langle\cdot\rangle = \frac{1}{4\pi}\int_0^{2\pi}\int_0^{\pi}(\cdot)sin(\phi)d\phi d\theta$ denotes the average operation by countering all propagation directions. We adopt this mean dispersion measure to minimize the impact of propagation direction by averaging over the RVE. This measure allows us to focus the discussion of numerical dispersion primarily on the chosen time integration scheme and the CFL number, especially within the context of homogenization.

The adoption of global mean dispersion greatly facilitates the dispersion analysis presented in Section 4. Fig. 6(a) show the application of the global dispersion strategy $\langle \frac{c-c_0}{c_0} \rangle$ for four tested schemes at CFL equals to 0.7. Meanwhile, Fig. 6(b) displays the global mean dispersion for Scheme IV across various CFL values. It is observed that each scheme exhibits distinct dispersion for a given CFL number (Fig. 6(a)). Moreover, both excessively low and high CFL values contribute to significant dispersion errors (Fig. 6(b)), which we have confirmed for all four schemes. Similar analyses are performed in Section 4 without the necessity of discussing local propagation direction dispersion at the microscale.

3.2. Stability analysis and dissipation

We address here the dispersion linked to the stability and dissipation by the time integration schemes, which we had left out of the previous discussion. The time integrator introduces a finite difference discretization into the time domain, as shown in Eq. (32), which can induce parasitic modes [63], even when full integration is applied within the FEM framework. Green's function, in this context, generates singular responses along with the main wave components, which can worsen due to this issue. This justifies the selection of the α-method family as the analysis starting point, due to its parameter-dependent damping coefficient. The analysis of the stability and dissipation for the α-method has been thoroughly discussed in previous studies [58,64]. To facilitate the discussion of stability and numerical dissipation for the four tested schemes, it is beneficial to modify Eq. (15a) for a single-degree-of-freedom system as follows:

$$\ddot{u} + 2\xi\omega\dot{u} + \omega^2 u = 0, \tag{34}$$

where ξ represents the damping ratio. Eq. (34) can also be considered as the mass-normalized form of Eq. (10) for a specific mode. The α-method's dissipation and stability can be evaluated through a compact form [58]:

$$\mathbf{X}_{n+1} = \mathbf{A}\mathbf{X}_n, \tag{35}$$

where $\mathbf{X}_n = \{u_n, \Delta t\dot{u}_n, \Delta t^2\ddot{u}_n\}$. Here, $\mathbf{A}$ is the amplification matrix determined by the time integration scheme. The formulation for the corresponding spectrum radii and damping has been extensively explored in [58]. In the context of the schemes discussed in this paper, the spectrum radius is defined by the maximum eigenvalues $\rho_s = \max\{|\lambda_i|\}$ of the amplification matrix, as shown in Fig. 7(a). It is demonstrated that all schemes are unconditionally stable (i.e., $\rho_s \leq 1$ for $\forall\ \Delta t/T\ > 0$).

The dissipation or damping can be represented by the function $\xi = \xi(\Delta t/T)$. Referring to the example schemes listed in Table 1, their damping characteristics are illustrated in Fig. 7(b). By enhancing the α parameter, through Scheme I to III, the damping ratio increased, particularly in the range of approximately $\Delta t/T \in [0, 1]$. However, for higher wave modes where $\Delta t/T > 1$, the numerical

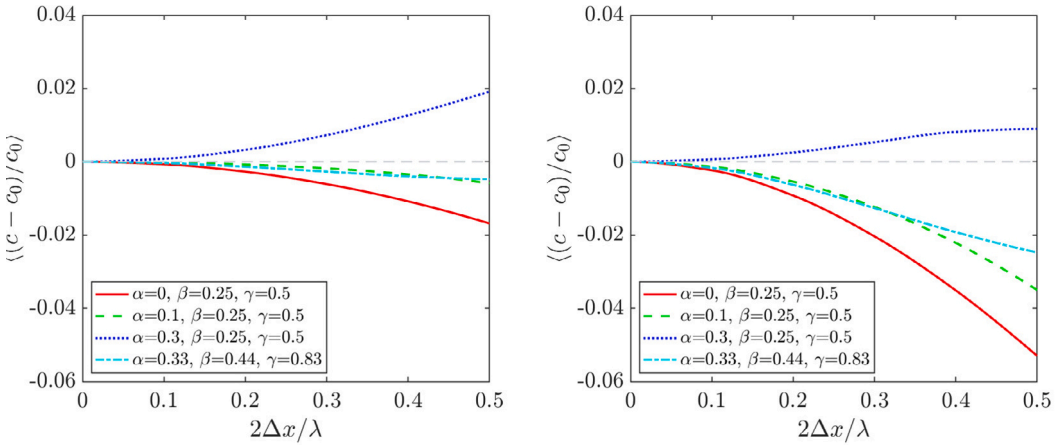

(a) Time integration schemes (Left: $CFL = 0.7$. Right: $CFL = 1.0$).

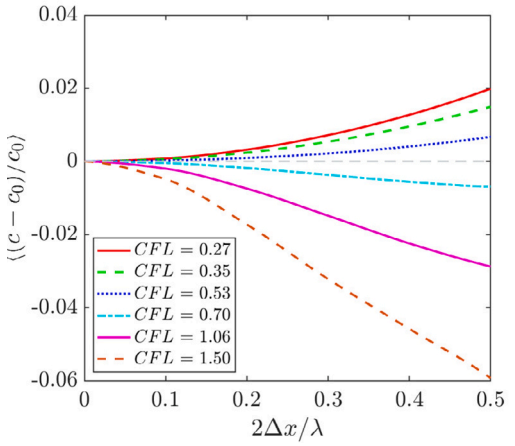

(b) $CFLs$ (Scheme IV).

Fig. 6. The global mean dispersion based on the grid dispersion analysis for different: (a) Time integration schemes; (b) $CFLs$.

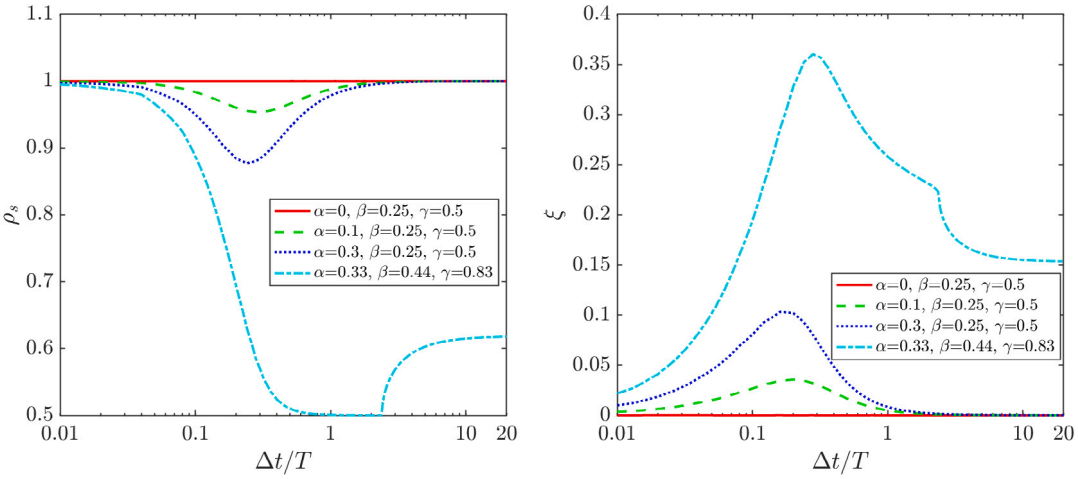

(a) Spectrum radii. (b) Damping ratio.

Fig. 7. Time step stability and damping ratio for different time integration schemes.

damping effect introduced by the α parameter quickly diminishes. The influence of β and γ parameters is significant as they not only increase dissipation for the relatively low-frequency part where $\Delta t/T < 1$, but they also maintain sufficient dissipation in the high-frequency domain when $\Delta t/T > 1$.

In Section 3.1, we have emphasized the numerical dispersion error associated with the CFL number, which can be illustrated as a function of normalized wavelength $2\Delta x/\lambda$. It should be noted that $\Delta t/T = 4\Delta x/\lambda$ by recalling the relationship $c_0 = \lambda/T$. To further show its impact on the numerical dissipation, let us take the hexahedral element as an example and consider the range of non-zero elemental frequencies

$$\omega^e \in [\frac{2\sqrt{3}c_0}{\Delta x}, \frac{6c_0}{\Delta x}], \quad \omega^e_{max} = \frac{6c_0}{\Delta x}, \tag{36}$$

where the equidistant discretization and full integration are employed herein and the scalar wave problem (Eq. (23)) is referred to. The maximum elemental frequency indicates the upper bound of ω_n [65], then we will have the limit of $\frac{\Delta t}{T}$

$$\frac{\Delta t}{T} \in [0, \frac{\omega_{\max}\Delta t}{2\pi}], \quad \frac{\Delta t}{T} \in [0, \frac{3CFL}{\pi}], \tag{37}$$

Eq. (37) demonstrates that the limit of $\frac{\Delta t}{T}$ is governed by the CFL number. Given that the damping curves for a specific scheme are considered constant, reducing the CFL number leads to low-frequency wave modes experiencing weaker dissipation. This issue means mitigating the dispersion error that may cause under or over-dissipation on parasite modes. Finally, recalling Nyquist frequency, we denote a normalized frequency measure $\hat{\omega}$ for indicating the range of $\Delta t/T$ in sampling time histories:

$$\hat{\omega} \in [0, \frac{1}{2}]. \tag{38}$$

The normalized frequency $\hat{\omega}$ is useful in aligning the comparisons for the dispersion and numerical dissipation, which is employed in all following numerical tests throughout Section 4.

4. Numerical tests

This section presents a series of numerical tests designed to illustrate and evaluate the proposed approach and to explore the parameter landscape for optimal performance. The FEM formulation is developed and implemented in the open-source computational framework MOOSE (Multiphysics Object-Oriented Simulation Environment). Thanks to the well-established parallel FEM framework by MOOSE and our custom implementations [66–68], all computations are executed using MPI (Message Passing Interface) to ensure optimal scalability. These processes are facilitated by the ROAR Collab Cluster, a high-performance research computing cluster managed by the Institute for Computational and Data Sciences (ICDS) at Penn State.

4.1. Influence of numerical damping

This section examines the effects of varying numerical damping on solving Green's function. The problem is modeled within a 3D, infinite, homogeneous medium. We conducted this numerical test using a cubic domain, each side measuring 1.0×10^{-3} length units. At the cube's center, a unit point impulse source $\mathbf{x}'$ is positioned at $[0.5, 0.5, 0.5] \times 10^{-3}$. The spatial domain is discretized using a $100 \times 100 \times 100$ structured grid with equidistant spacing. The temporal discretization is achieved through a time step which size is calculated accordingly to the target CFL numbers (0.27, 0.53, 0.71 and 1.06, with theoretical transverse and longitudinal wave speeds of 0.7071 and 1.0). The time step is maintained constant throughout the time domain. The material properties used in the simulation include a Young's modulus of 1.0, a Poisson's ratio of 0.0, and a density of 1.0. To approximate the infinity of space, we limit the time range of the simulation to avoid reflections (natural boundary conditions), ensuring that no essential boundary conditions are enforced. This approach allows us to focus on the direct impact of numerical damping in an idealized infinite medium.

The effect of numerical damping can be illustrated by Fig. 8(a)–(d) by different time integration schemes. The space–time solutions $G_{11}(\mathbf{x}, \mathbf{x}', t)$ on the principal plane y-z where the component of position vector $x = 0$ and same time instance are selected for comparison. The displacement is normalized by the greatest magnitude of the responses, which is used for all plotted wave profiles in this study. As depicted in Fig. 8(a), the wave profile by the Newmark-beta scheme with zero numerical damping shows significant oscillations, where the magnitude of each oscillated phase is nearly the same. These high-frequency modes are consistent with the published observations [53,61]. Fig. 8(b)–(c) examine the oscillations that can be gradually suppressed by enhancing the α parameter. Notably, in Fig. 8(d), we observe that no distinct oscillations are achieved when sufficient numerical damping is introduced through γ and β parameters.

Fig. 9(a)–(d) presents the effects of numerical dissipation as observed in the transformed p-space solutions, where the peak represents now the transverse component p_T. The application of spatial Fourier transform is shown to effectively separate oscillations, particularly in the range of artificial wave components across wide wave numbers. The results indicate a similar response to the increase of numerical damping. Additionally, Fig. 10(a) provides a closer look at the solutions related to a single wave vector $\hat{\mathbf{p}}$. Here, the trapezoidal rule results in the emergence of multiple peaks over a wide range of p. As numerical damping increases, it becomes evident that the ripples, especially those with wave numbers $p > p_T$, are smoothed out. However, it is important to note that numerical damping has a limited effect on suppressing the wave component when $p < p_T$. Recalling the phase speed equation, we will find that numerical dissipation can only dampen out the artificial wave where the propagation speed is slower than c_T. As demonstrated in Fig. 7(b), this can be attributed to the minimal numerical damping in the low-frequency region.

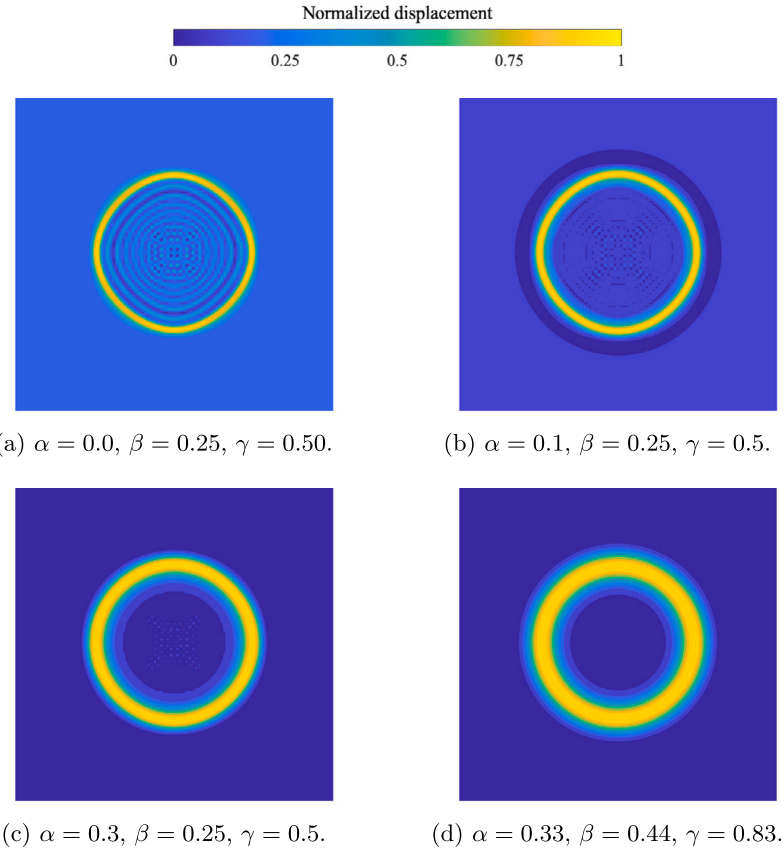

Fig. 8. The effect of α for numerical damping on space–time solutions ($CFL^T \approx 0.71$, taken at the same time instance): (a) $\alpha = 0.0$, $\beta = 0.25$, $\gamma = 0.50$; (b) $\alpha = 0.1$, $\beta = 0.25$, $\gamma = 0.5$; (c) $\alpha = 0.33$, $\beta = 0.25$, $\gamma = 0.5$; (d) $\alpha = 0.33$, $\beta = 0.44$, $\gamma = 0.83$.

Due to the best smoothness achieved by scheme IV among all tested four schemes, we take it as the example to show the influence of CFL (i.e., the spatial and temporal domain spacing) on the dissipation. Fig. 11(a)–(c) depict the space–time wave profiles under different CFL numbers. These variations in $CFLs$ are achieved by refining the temporal discretization while keeping the TI parameters and spatial discretization unchanged. As indicated by Eq. (37), reducing the CFL number will narrow the structural damping over the lower bound of $\Delta t/T$, which can reduce the numerical dissipation. However, it can be observed that the oscillated wave profiles all become hard to distinguish when Scheme IV is employed. Fig. 12(a)–(c) showcased the corresponding p-space profiles where Fig. 10(b) checked one specific propagation direction. It examines additionally trivial artificial wave components ($p > p_T$) that will happen when CFL is refined to 0.27.

In summary, this section highlights the crucial role of numerical dissipation in solving the numerical Green's function. We have demonstrated that increased numerical dissipation can effectively suppress artificial wave components. Furthermore, our numerical analysis confirms that refining the CFL number could potentially decrease dissipation, as predicted in Section 3.2. However, this search for an optimal CFL number might come with the trade-off of introducing more parasitic modes into the modeled wave.

4.2. CFL number role in the wave speed measurement

Measuring acoustic speed is a major objective in wave propagation analysis. This section investigates the impact of spatial and temporal discretization (via CFL number) in the accurate measurement of acoustic speeds. The model and simulation parameters used in Section 4.1 are inherited here, being the theoretical transverse and longitudinal wave speeds 0.7071 and 1.0, respectively. The characterization scheme proposed in Section 2.3 is employed for space–time and transformed p-space solutions.

Table 2 presents the specific spatial and temporal discretizations employed, along with the wave speed measurements derived from space–time Green's function solutions. In this analysis, only Scheme IV is considered, owing to its ability to produce non-oscillated space–time profiles as discussed in Section 4.1. The results indicate that within the CFL range for both longitudinal (CFL^L) and transverse (CFL^T) waves, spanning from 0.27 to 1.06, our methodology achieves wave speeds that maintain a high level of accuracy, with relative errors not exceeding 3%. The space–time measurements result in consistent wave speeds across a broad range of CFL values. Note however that, as the CFL value goes above 1.0, a noticeable underestimation is observed. Conversely, extremely low values, such as $CFL = 0.27$, lead to an overestimation of the wave speeds.

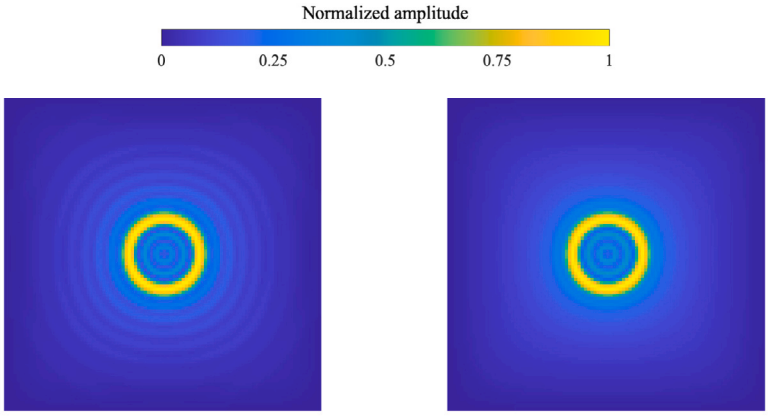

(a) $\alpha = 0.0,\ \beta = 0.25,\ \gamma = 0.50.$ (b) $\alpha = 0.1,\ \beta = 0.25,\ \gamma = 0.5.$

(c) $\alpha = 0.3,\ \beta = 0.25,\ \gamma = 0.5.$ (d) $\alpha = 0.33,\ \beta = 0.44,\ \gamma = 0.83.$

Fig. 9. The effect of α for numerical damping on p-space solutions ($CFL^T \approx 0.71$, $\hat{\omega} \approx 0.16$): (a) $\alpha = 0.0$, $\beta = 0.25$, $\gamma = 0.50$; (b) $\alpha = 0.1$, $\beta = 0.25$, $\gamma = 0.5$; (c) $\alpha = 0.33$, $\beta = 0.25$, $\gamma = 0.5$; (d) $\alpha = 0.33$, $\beta = 0.44$, $\gamma = 0.83$.

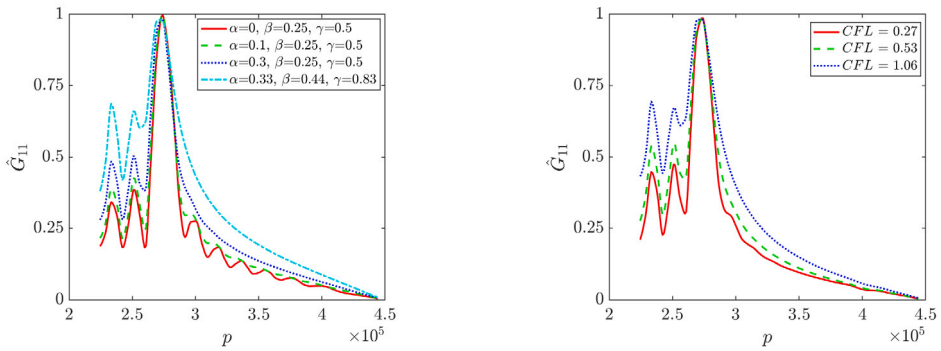

(a) time integration schemes. (b) CFL number (by Scheme IV).

Fig. 10. The normalized p-space profile $\tilde{G}_{11}$ affected by: (a) time integration schemes; (b) CFL numbers (by Scheme IV).

Table 2
A CFL number test based on the Scheme $\alpha = 0.33$, $\beta = 0.44$, $\gamma = 0.83$.

Case	$NCells$	Δ × (×1.0e^{-5})	Δt(×1.0e^{-5})	CFL^L	CFL^T	c_L	c_T
1	100	1.0	1.0	1.0	0.71	0.976	0.703
2	100	1.0	0.5	0.5	0.35	0.998	0.709
3	150	0.66	1.0	1.5	1.06	0.966	0.682
4	150	0.66	0.5	0.75	0.53	1.007	0.704
5	150	0.66	0.25	0.35	0.27	1.040	0.711

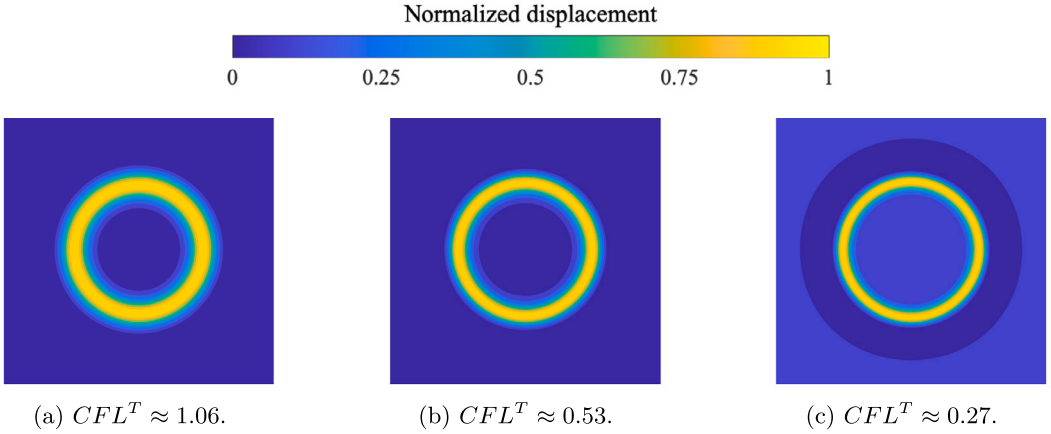

Fig. 11. The effect of CFL number for numerical damping on space–time solutions ($\alpha = 0.33$, $\beta = 0.44$, $\gamma = 0.83$, taken at the same time instance, spatial discretization unchanged): (a) $CFL^T \approx 1.06$; (b) $CFL^T \approx 0.53$; (c) $CFL^T \approx 0.27$.

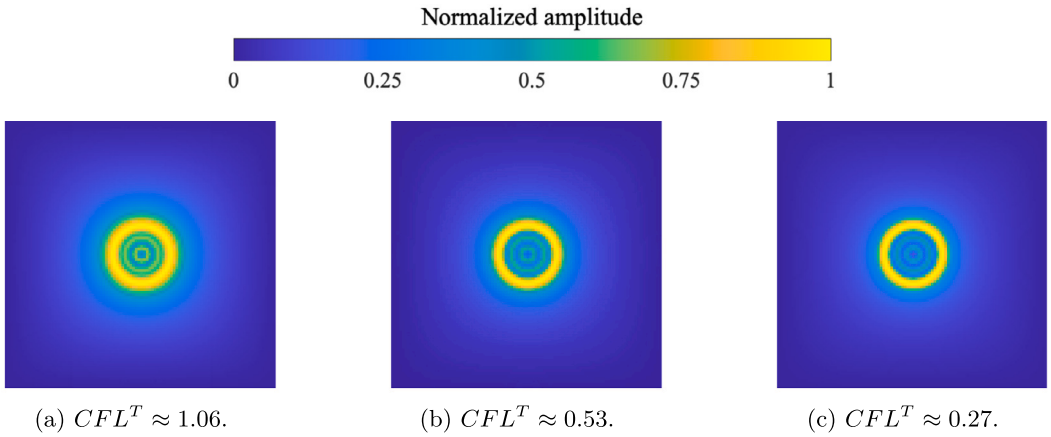

Fig. 12. The effect of CFL number for numerical damping on p-space solutions ($\alpha = 0.33$, $\beta = 0.44$, $\gamma = 0.83$, $\hat{\omega} \approx 0.16$, spatial discretization unchanged): (a) $CFL^T \approx 1.06$; (b) $CFL^T \approx 0.53$; (c) $CFL^T \approx 0.27$.

In the previous section, Fig. 10(a)–(b) examined a shift in the peak wave number that can be observed by different time integration schemes and CFLs due to the numerical dispersion. The quantitative results based on the global average are illustrated by Fig. 13(a)–(b). In these figures, ω and p denote the discrete frequency point and volumetric averaged peak wave number of the wave component, respectively. All sampled data points are depicted as scatter plots, with a fitted line employed to demonstrate their overall trend. The frequency ω is scaled and replaced by the normalized frequency $\hat{\omega}$ (see Section 3.2), and the x-axis is scaled accordingly, represented by the values of $2p\Delta t$. The slope of the fitted line is interpreted as an average of the phase velocity, illustrating the speed deviation across different schemes or CFL values. A notable trend observed in various time integration schemes is that an increase in numerical damping is associated with a rise in speed measurement. This finding is consistent with the global dispersion error plots shown in Fig. 6(a). Furthermore, Fig. 13(a) reveal that the principal wave number converges as the non-dimensional frequency nears zero. This convergence occurs because the dispersion of each scheme approaches zero when the normalized frequency is minimal. Moreover, Fig. 13(b) investigate the relationship between phase speed and increasing CFL values. The results support the predictions in Fig. 6(b), indicating that both very low and very high CFL values can lead to significant errors.

In the discussion above, we highlighted the significant effect of the CFL number on speed measurement accuracy. Using a homogeneous isotropic benchmark, we found that space–time speed measurements maintain satisfactory accuracy across a broad CFL range, with notable deviations occurring only when the CFL number is excessively high or overly refined. Moreover, through the $p - \omega$ relationship derived from transformed p-space solutions, we observed a strong correlation in the phase speed trends as predicted by the analysis of mean numerical dispersion associated with different CFL numbers. The discrepancies noted in space–time measurements could be due to parasitic modes that are not completely eliminated by numerical dissipation. However, p-space measurements remain consistent, as artificial waves are generally isolated and distributed across the p spectrum. By focusing solely on the average of the primary wave component, the results are likely less influenced by oscillatory modes.

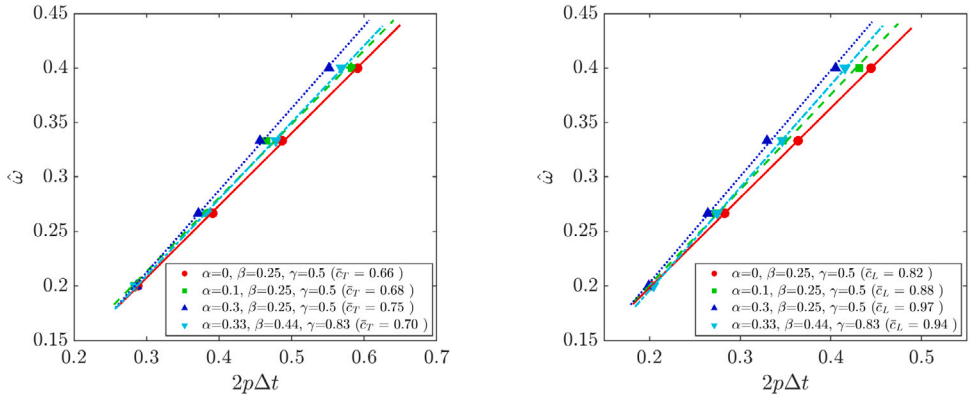

(a) time integration scheme.

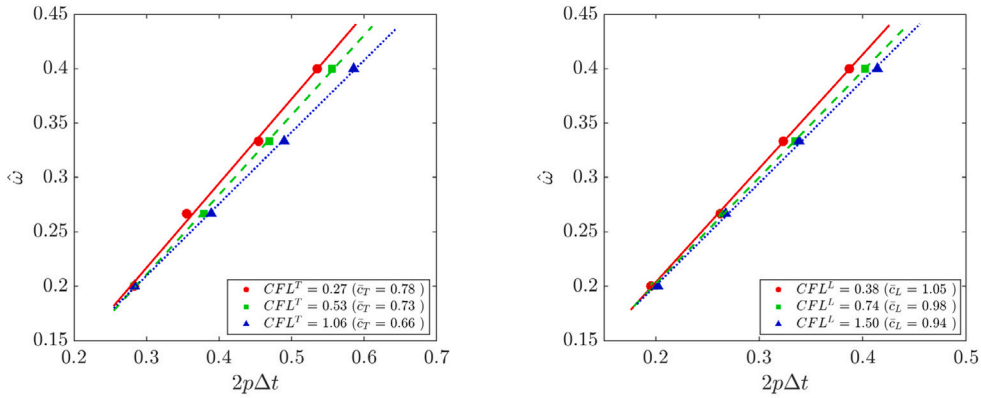

(b) $CFLs$ (Scheme IV).

Fig. 13. The speed deviation based on p-space solutions associated with (a) time integration scheme; (b) $CFLs$ (Scheme IV). Left column: transverse wave. Right column: longitudinal wave.

Table 3
The elasticity constants of single ice crystal [69] (unit: GPa).

C_{11}	C_{12}	C_{13}	C_{33}	C_{44}
13.94	7.08	5.76	15.00	3.01

4.3. Wave modeling and measurements for polycrystalline structures

This section illustrates a practical application of Green's function RVE approach, specifically for characterizing the acoustic properties of polycrystalline ice structures. It incorporates the lessons learned in previous analyses, and additionally, it cooperates with the discussion of numerical dispersion and spatial refinement. We utilize the elastic constants of a single ice crystal characterized as transversely isotropic material, as detailed in Table 3 [69]. The Zener anisotropy factor $A = 2c_{44}/(c_{11} - c_{12}) = 0.88$, which is a low anisotropic index (Isotropic material: $A = 1$). The density of the ice is set at 916.8 kg/m^3. The study by Gammon et al. [69] estimated the average isotropic longitudinal and transverse wave speeds within a single crystal using Simpson's rule, yielding values of 3844.94 m/s and 1956.9 m/s, respectively. These speeds were used to approximate the CFL numbers for the measured wave components.

Section 2.1 has discussed the generation and control of morphology for a quasi-equiaxed structure. We consider a representative ESD of the ice polycrystalline microstructure to be approximately 3.1 mm. The tested RVE sizes vary from 6.3 mm to 125 mm, correlating to a grain count per RVE ranging from 8 to 32,768, as shown in Fig. 14. We define the number of elements per ESD as $nele = ESD/\Delta x$, which represents the spatial refinement of the grain geometry. The grain orientations are assumed to follow a zero-mean random distribution, with the probability density function (PDF) adhering to the arc-cosine function [70]. We employed six groups of independently generated Euler angles to capture the variations in orientation. In line with our previous benchmark tests, our objective is to obtain Green's function in a 3D infinite space. To uphold the assumption of infinite space, we ensured that neither natural nor essential boundary conditions were applied.

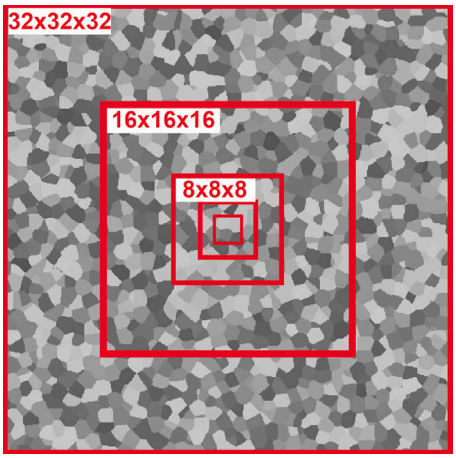

Fig. 14. A sketch for the RVE sizes that are investigated.

Table 4
A CFL number test for the polycrystalline structures.

Case	RVE size	CFL^T	CFL^L	$\bar{c}_T$ (m/s)	$\bar{c}_L$ (m/s)
1	$32 \times 32 \times 32$	0.10	0.18	1980.7	3890.7
2		0.19	0.36	1938.6	3830.0
3		0.39	0.77	1926.0	3850.1
4		0.78	1.54	1873.1	3889.9

In previous sections, we discussed the impact of the CFL number on numerical dispersion within a homogeneous isotropic medium. This effect is further examined in polycrystalline structures with homogenization. We refined the CFL number by maintaining constant spatial discretization (i.e., consistent refinement of grain geometry) and varying the time step. Table 4 displays the speed measurements derived from space–time solutions using Scheme IV. Scheme IV is favored herein due to its adequate dissipation where no additional treatment is needed to find the peak responses. For the transverse wave, space–time measurement increases as CFL^T is refined. Unlike the results discussed by Section 4.2, the space–time measurements tend to have no specific CFL range to show a consistent speed. Similar findings can be obtained by checking the longitudinal wave, however, a staggered or even contrary trend over the CFL number is shown. Specifically, as CFL^L is refined, the averaged $\bar{c}_L$ initially decreases and then increases. Correspondingly, Fig. 15(a)–(b) illustrate the $\hat{\omega} - 2p\Delta t$ curves. The trend of CFL^T concerning the fitted phase speed remains consistent for transverse waves. Conversely, for longitudinal waves, the phase speed exhibits an inverse relationship with CFL^L. This phenomenon suggests that numerical dispersion issues become more intricate in the context of a heterogeneous medium. Unlike homogeneous cases where a single optimal CFL value may suffice for all primary wave components, heterogeneous mediums might require distinct CFL values for each component. Notably, numerical dispersion can alter the timing of wave interactions with scatterers, potentially affecting the scattering mode and ultimately the homogenized results. Consequently, the accuracy of measured transverse wave components should be favored due to their greater consistency with the chosen CFL value and the accounted effects of numerical dispersion.

The impact of refining the discretization of grain geometries is examined, with a constant CFL maintained across all cases to minimize the influence of numerical dispersion. In the generated polycrystalline microstructures, spatial refinement will result in a more detailed tessellation of grain boundaries, as indicated by the ratio $nele$. This analysis aims to assess how such refinement affects the averaging of acoustic properties. Table 5 presents the speeds derived from space–time solutions using Scheme IV, showing that refinement leads to minimal variation in measured values—less than 1% fluctuation across $nele$ values from 7.75 to 31. This similarity is likely due to the relatively equiaxed nature of the polycrystals and the low anisotropy of the single crystals examined (Table 3, $A = 0.88$). Notably, a decreasing trend in space–time measurements becomes apparent as grain geometry is refined beyond $nele = 15.5$. Literature suggests that $nele \geq 10$ should be recommended [2,37]. Analytical methods [2] have shown that the two-point correlation function, as modeled by FEM, achieves satisfactory accuracy at $nele = 10$, with further refinement yielding negligible improvements, particularly for near-field measurements, and only a slight increase in two-point correlation for far-field observations with additional refinement of $nele$. Hence, the low fluctuation observed in Table 5 can be justified. The observed decreasing trend is likely due to the increased resolution in spatial or temporal discretization. Nonetheless, for crystals with more complex shapes or higher anisotropy, the impact of grain boundary resolution on measurement accuracy requires further investigation. Moreover, Fig. 16(a)–(b) present the effect of grain geometry refinement in the p-space measurement. Fitted trends of each $nele$ case show great similarities where the magnitude of slope deviates less than 5%. This examined the homogenized results tend to show almost a convergence at current grain discretization where minimum $nele = 7.75$.

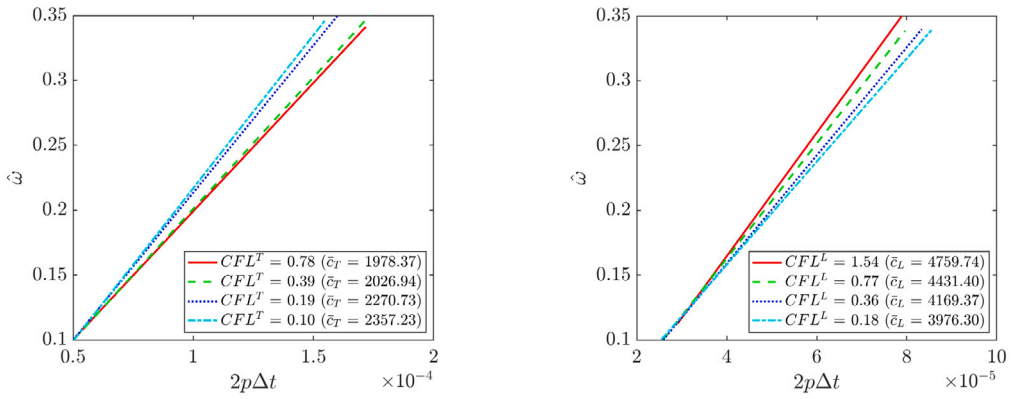

(a) Transverse wave. (b) Longitudinal wave.

Fig. 15. The speed deviation based on p-space solutions associated with CFL numbers: (a) Transverse wave; (b) Longitudinal.

Table 5
The influence from the resolution of discretized grain boundary for the polycrystalline structures.

Case	RVE sizes	*nele*	$\Delta x(\times 1.0e^{-4})$	$\Delta t(\times 1.0e^{-7})$	c_T (m/s)	c_L (m/s)
1	8 × 8 × 8	7.75	5.0	1.0	1893.6	3860.8
2		15.5	2.5	0.50	1898.2	3865.2
3		20.7	1.875	0.375	1895.8	3863.9
4		31	1.25	0.25	1891.1	3855.2

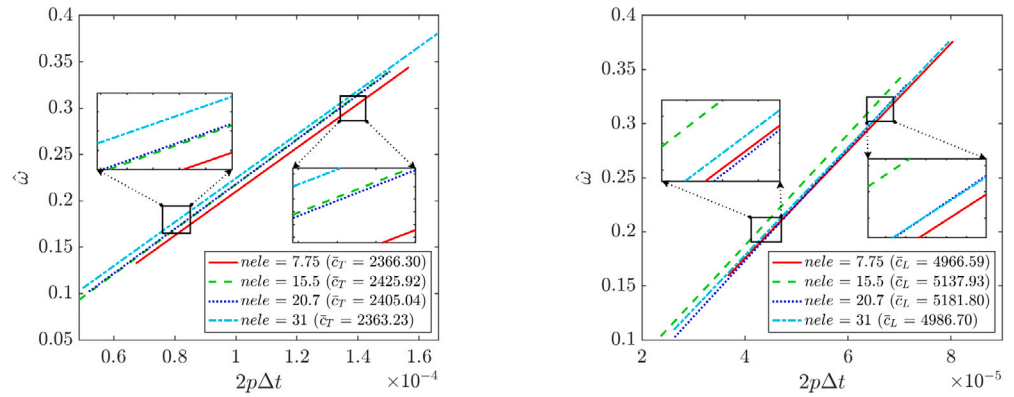

(a) Transverse wave. (b) Longitudinal wave.

Fig. 16. The speed deviation based on p-space solutions associated with spatial discretizations: (a) Transverse wave; (b) Longitudinal.

The size effect of RVEs by using different time integration schemes is then investigated. Each case is discretized with a consistent CFL number. To save computational cost, we ensure the *nele* at least be 7.75 as discussed above. Fig. 17(a)–(d) illustrate the transverse wave space–time profiles at $t = n^{grains} t_1$ by using Scheme I–IV, respectively. The RVE size and the timing of each snapshot are proportionally scaled, thus resulting in analogous wave profiles. In the absence of numerical dissipation, Fig. 17(a) reveals the distinct oscillations consistent across all sample sizes. Conversely, with the introduction of increased numerical dissipation, Fig. 17(b)–(d) show progressively smoother transverse wave profiles.

Additionally, we report that, in the case of heterogeneous media, as depicted in Fig. 17(a)–(c), certain wavefronts propagate faster than the primary wave due to insufficient numerical dissipation. These wavefronts, comparable in magnitude to the primary transverse wave, complicate the measurement of space–time solutions. This discrepancy may stem from the substantial difference in CFL numbers for P- and S-waves within the anisotropic model under consideration, resulting in decreased dissipation for transverse waves and, thus, more noticeable oscillations. This observation suggests that when dealing with significant speed ratios in anisotropic models, particular attention should be paid to these parasitic modes. Furthermore, examining the 2 × 2 × 2 or 8 × 8 × 8 groups in Fig. 17(a), we identify distinct wavefronts that travel much faster than the primary wave. As demonstrated in Fig. 17(b)–(d), these faster phases become progressively smoothed as dissipation increases. In addition to the numerical oscillation issues, the 2 × 2 × 2 RVE typically exhibits the most distorted transverse wave profile due to the single scattering. As the wave interacts with a sufficient

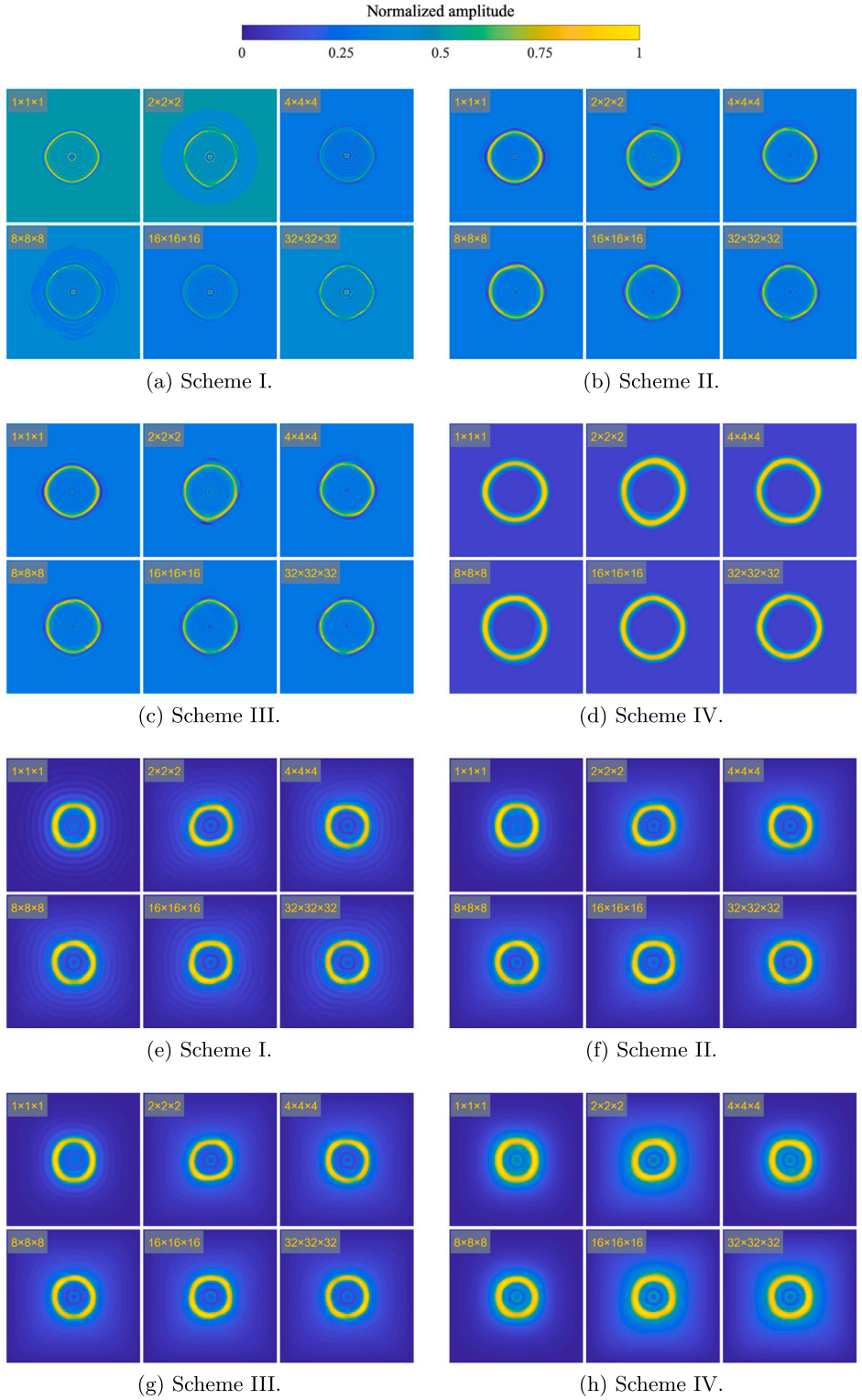

(a) Scheme I. (b) Scheme II.

(c) Scheme III. (d) Scheme IV.

(e) Scheme I. (f) Scheme II.

(g) Scheme III. (h) Scheme IV.

Fig. 17. The space–time (a–d) and p-space (e–h) profiles for varied RVE sizes by measuring G_{11} on YOZ plane using different time integration schemes.

Table 6
The space–time speed measures for varied RVE sizes by Scheme IV.

Case	RVE sizes	*nele*	c_L (m/s)	c_T (m/s)
1	2 × 2 × 2	62	1855.5	3797.3
2	4 × 4 × 4	31	1891.2	3790.4
3	8 × 8 × 8	31	1891.1	3855.2
4	16 × 16 × 16	15.5	1937.3	3855.1
5	32 × 32 × 32	7.75	1926.0	3850.1

number of grains, inducing multiple scatterings, these distortions are diminished, leading to wave profiles that exhibit isotropy or directional independence. Table 6 shows the speed measurement by evaluating the space–time solutions from Scheme IV. Notable discrepancies are observed primarily in the smaller RVE sizes for Cases 1 and 2. However, beginning with Case 3, both longitudinal and transverse speeds show minimal variation with the increase in RVE size.

Fig. 17(e)–(h) exhibit the p-space profiles for various RVE sizes on the principal plane yOz by Scheme I–IV, respectively. Across different sample sizes, the trapezoidal rule shows artificial wave components spanned for wide wave numbers (Fig. 17(e)). In comparison, Fig. 17(f)–(h) demonstrate increasingly smoothed profiles achieved by enhancing numerical dissipation, a trend consistent with the isotropic case discussed in Section 4.1. However, enhancing dissipation is still proved inefficient for suppressing the oscillations where the wave number p is smaller than the primary component. The p-space profiles further illustrate the process of homogenization across increasing length scales. In single ice crystals, notable symmetry reflects the material's homogeneity, which diminishes in polycrystalline media due to scattering. As RVE sizes increase, the primary wave component depicted in the p-space profile assumes a circular shape, indicating directional independence. Correspondingly, the $p-\omega$ relationship by each scheme is presented in Fig. 18(a)–(d). For Scheme I–III (Fig. 18(a)–(c)), the speed immediately converged even for the oligocrystalline structures. The averaged transverse wave component exhibits a consistent mean phase speed from the smallest RVE size. In contrast, longitudinal waves display a sudden increase in speed within the 2 × 2 × 2 group and become independent on the length scale starting from the 4 × 4 × 4 group onwards. Additionally, an increase in the α parameter significantly reduces the speed deviation in the longitudinal wave component for the smallest oligocrystalline group, from about 12% in Scheme I to just 3% in Scheme III. In Scheme IV (Fig. 18(d)), significant variations in the mean phase speed are evident for RVE sizes 4 × 4 × 4 and 8 × 8 × 8, with larger samples yielding mean phase speeds that more closely align with those observed in oligocrystalline cases. In summary, length scale-related convergence is noticeable across the different time integration schemes. However, the trend of variation for each wave component and time integrator differs. For homogeneous isotropic cases, the $p-\omega$ relationship appears unaffected by parasitic modes, as discussed in Section 4.2. This suggests that parasitic modes become more intricate in heterogeneous cases, particularly when considering limited scattering behavior.

5. Conclusions

Prior work has investigated the effectiveness of plane wave modeling in homogenizing the acoustic properties of heterogeneous medium. In this paper, we propose a Green's-function-based characterization scheme cooperating with representative volume elements for determining the acoustic properties. Compared with plane wave modeling, this scheme does not need extra assumptions on the macroscopic displacement field, which can be attractive in capturing wave behaviors at different scales or homogenizing textured materials. Moreover, it shows the possibilities for characterizing the broadband wave which can greatly reduce the computational cost in wave modeling. Besides these advantages, we also point out the potential challenges in numerically calculating Green's function with homogenization, especially the issues from the parasite modes and the numerical dispersion for the waves showing broadband frequencies.

We found that numerical damping or further treatment can be necessary for analyzing calculated Green's solutions while it can enhance the amplitude in attenuation discussion. For space–time Green's function, oscillated wave profiles are observed in both homogeneous and heterogeneous mediums when no numerical damping is introduced. When oscillations are transformed to the p-space, the nonphysical amplitude will be captured at non-principal wave numbers within a wide range. Through homogeneous medium benchmarks, numerical damping is determined to help smooth these parasite modes for wave numbers that are greater than the principal waves. However, the most dissipated time integration scheme is found unable to dampen out the component where wave numbers are smaller than the principal waves. This may be due to the introduced numerical damping is generally trivial at low frequencies.

The spatial and temporal discretization is tested which can greatly affect the accuracy of acoustic speed, even for the heterogeneous medium. For a specific approximation scheme, the CFL number defined by $\frac{c_0 \Delta t}{\Delta x}$ is tested crucial for the accuracy of modeled wave speeds by the homogeneous isotropic benchmarks, which are consistent with the prior studies. Numerical dispersion is generally small for the low-frequency part while it unavoidably deviates more from the physical wave speed, which is the same in four tested schemes. Considering the phase speed of low frequency is an alternative approach to alleviate the influence of numerical dispersion. The potential to weaken the numerical dissipation by refining CFL is also proven and discussed. Furthermore, we propose using global dispersion error by averaging all propagation directions for the calculated spherical waves and averaging the acoustic properties. The numerical results showed that adjusting the CFL numbers to be optimal in global dispersion error can effectively improve the accuracy of the volumetric averaged speed measurements. Moreover, we investigated the influences of the

(a) Scheme I

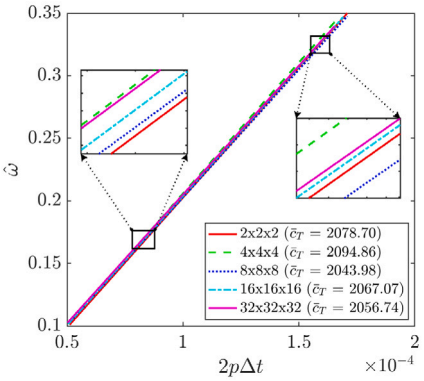

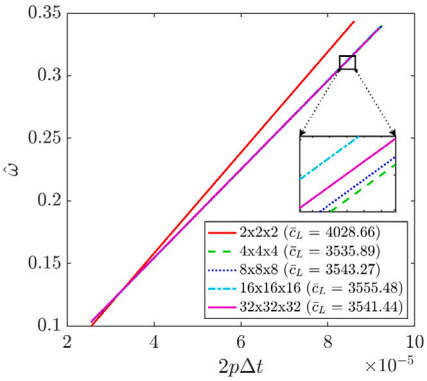

(b) Scheme II

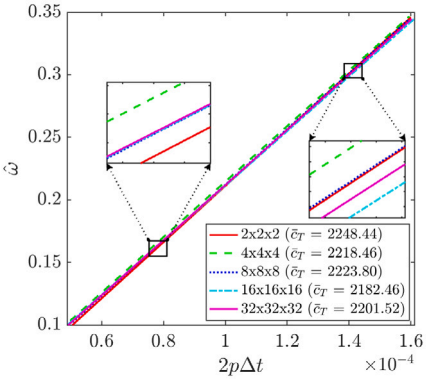

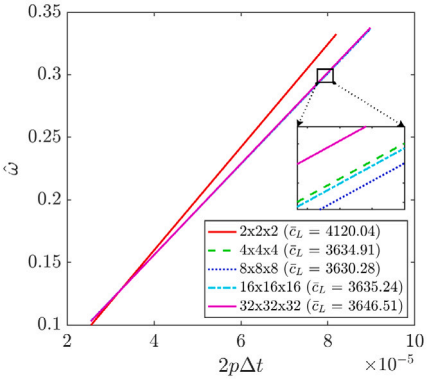

(c) Scheme III

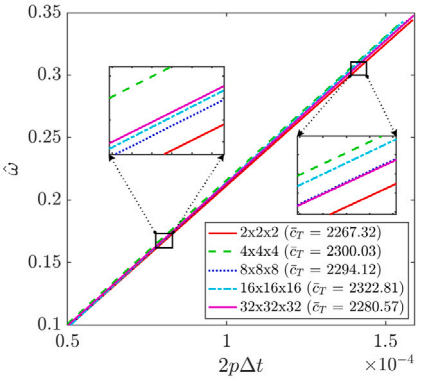

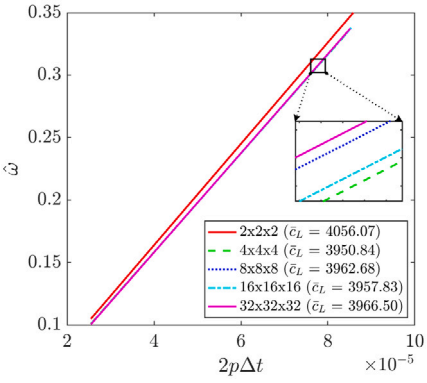

(d) Scheme IV

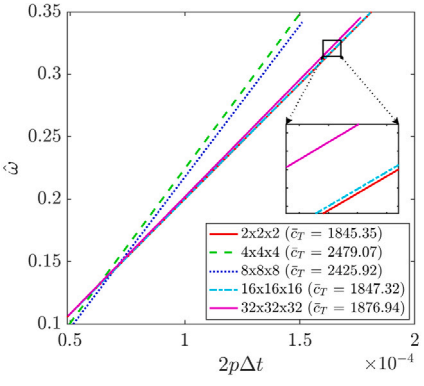

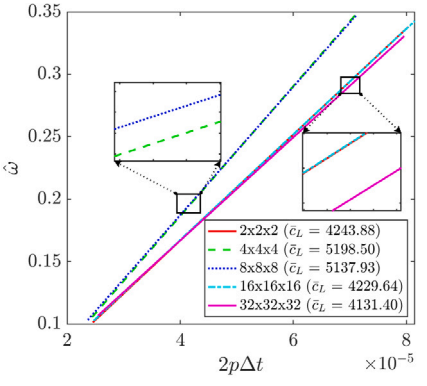

Fig. 18. The speed deviation based on p-space solutions associated with RVE sizes by: (a) Scheme I; (b) Scheme II; (c) Scheme III; (d) Scheme IV;.

$CFLs$ in homogenizing the heterogeneous mediums. The transverse wave component exhibits a consistent trend associated with the CFL number in the isotropic benchmark test. While the longitudinal wave for the heterogeneous medium can show a contrary trend.

In characterizing the complex microstructures, we combined the analysis with the numerical dispersion, sample size effect, and refinement on spatial discretization. We noted that careful considerations are required for controlling the final averaged measurements. For polycrystalline ice structures, we employed the quasi-equiaxed morphology and showed the anisotropy is gradually diminished by long-range wave propagation. Refining the geometry of the microstructure is shown to exhibit the difference for the high-frequency part, but the measures by using the space–time measure got almost the same speeds.

Besides the findings obtained in this paper, we emphasize the following topics that may be attractive in future investigation: First, we numerically revealed the impact of smoothing out the parasite modes in homogenizing the heterogeneous medium properties. However, it is still necessary to provide a quantitative analysis by countering the multi-scattering with those high-frequency oscillations. This may be inspiring in further developing a more well-rounded scheme in modeling the broadband frequency waves and homogenization process. Second, note that this work considers all wave frequencies, wave numbers, etc. as real numbers. Although numerical dissipation helps in damping oscillated responses, it is not adequately discussed quantitatively. When dealing with dissipation or attenuation, a detailed measurement by considering both the constitutive dissipation and numerical damping should be proposed. Beyond the direct volumetric average, some schemes that can minimize the global error for the fitted statistical isotropic or anisotropic material can also be very helpful. Finally, it can be interesting to focus on the low-frequency part where the dispersion and numerical dissipation are small because of the avoidable deviation on physical dispersion and attenuation. A wavelet with a specific principal frequency may be used to substitute the original point load scheme.

CRediT authorship contribution statement

Feihong Liu: Writing – original draft, Visualization, Software, Methodology, Investigation, Formal analysis. **Andrea P. Argüelles:** Writing – review & editing, Supervision, Resources, Project administration, Investigation, Funding acquisition, Formal analysis, Conceptualization. **Christian Peco:** Writing – review & editing, Supervision, Software, Resources, Project administration, Investigation, Funding acquisition, Conceptualization.

Declaration of competing interest

The authors declare that they have no known competing financial interests or personal relationships that could have appeared to influence the work reported in this paper.

Data availability

Data will be made available on request.

Acknowledgments

This material is based upon work supported by the National Science Foundation under Grant 2029142. Any opinions, findings, conclusions, or recommendations expressed in this material are those of the authors and do not necessarily reflect the views of the National Science Foundation. Computations for this research were performed on the Pennsylvania State University's Institute for Computational and Data Sciences' Roar supercomputer.

References

[1] Isaac Segovia Ramírez, Fausto Pedro García Márquez, Mayorkinos Papaelias, Review on additive manufacturing and non-destructive testing, J. Manuf. Syst. 66 (2023) 260–286, Elsevier.
[2] G. Sha, M. Huang, MJS Lowe, SI Rokhlin, Attenuation and velocity of elastic waves in polycrystals with generally anisotropic grains: Analytic and numerical modeling, J. Acoust. Soc. Am. 147 (4) (2020) 2442–2465, AIP Publishing.
[3] C. Kohlhauser, Ch Hellmich, Ultrasonic contact pulse transmission for elastic wave velocity and stiffness determination: Influence of specimen geometry and porosity, Eng. Struct. 47 (2013) 115–133, Elsevier.
[4] Jiang GUO, Haiyang FU, Bo PAN, Renke KANG, Recent progress of residual stress measurement methods: A review, Chin. J. Aeronaut. 34 (2) (2021) 54–78, Elsevier.
[5] Xiaobin Li, Jianguo Yan, Qiaomu Qi, Rui Xie, Characteristics of elastic wave dispersion and attenuation induced by microcracks in complex anisotropic media, J. Geophys. Eng. 18 (5) (2021) 788–807, Oxford University Press.
[6] F. Simonetti, M. Fox, Experimental methods for ultrasonic testing of complex-shaped parts encased in ice, NDT E Int. 103 (2019) 1–11, Elsevier.
[7] Sérgio H. Faria, Ilka Weikusat, Nobuhiko Azuma, The microstructure of polar ice. Part II: State of the art, Microdyn. Ice 61 (2014) 21–49, Elsevier.
[8] Meysam Toozandehjani, Khamirul Amin Matori, Farhad Ostovan, Faizal Mustapha, Nur Ismarrubie Zahari, Arshin Oskoueian, On the correlation between microstructural evolution and ultrasonic properties: a review, J. Mater. Sci. 50 (2015) 2643–2665, Springer.
[9] Ana Lopez, Ricardo Bacelar, Inês Pires, Telmo G. Santos, José Pedro Sousa, Luísa Quintino, Non-destructive testing application of radiography and ultrasound for wire and arc additive manufacturing, Addit. Manuf. 21 (2018) 298–306, ELsevier.
[10] Fred E. Stanke, Gordon S. Kino, A unified theory for elastic wave propagation in polycrystalline materials, J. Acoust. Soc. Am. 75 (3) (1984) 665–681, Acoustical Society of America.
[11] Woldemar Voigt, Lehrbuch der Kristallphysik: (Mit Ausschluss der Kristalloptik), vol. 34, BG Teubner, 1910.

[12] András Reuß, Berechnung der fließgrenze von mischkristallen auf grund der plastizitätsbedingung für einkristalle, ZAMM-J. Appl. Math. Mech./Z. Angew. Math. Mech. 9 (1) (1929) 49–58, Wiley Online Library.
[13] Richard Hill, The elastic behaviour of a crystalline aggregate, Proc. Phys. Soc. Sect. A 65 (5) (1952) 349, IOP Publishing.
[14] R. Hill, Elastic properties of reinforced solids: Some theoretical principles, J. Mech. Phys. Solids 11 (5) (1963) 357–372.
[15] E. Sanchez-Palencia, Homogenization method for the study of composite media, in: Asymptotic Analysis II, Springer, 1983, pp. 192–214.
[16] Senthil S. Vel, Alden C. Cook, Scott E. Johnson, Christopher Gerbi, Computational homogenization and micromechanical analysis of textured polycrystalline materials, Comput. Methods Appl. Mech. Engrg. 310 (2016) 749–779, Elsevier.
[17] Andrea P. Arguelles, Joseph A. Turner, Ultrasonic attenuation of polycrystalline materials with a distribution of grain sizes, J. Acoust. Soc. Am. 141 (6) (2017) 4347–4353, AIP Publishing.
[18] Frank C. Karal Jr., Joseph B. Keller, Elastic, electromagnetic, and other waves in a random medium, J. Math. Phys. 5 (4) (1964) 537–547, American Institute of Physics.
[19] R.L. Weaver, Diffusivity of ultrasound in polycrystals, J. Mech. Phys. Solids 38 (1) (1990) 55–86, Elsevier.
[20] RC Bourret, Propagation of randomly perturbed fields, Can. J. Phys. 40 (6) (1962) 782–790, NRC Research Press.
[21] RC Bourret, Stochastically perturbed fields, with applications to wave propagation in random media, Il Nuovo Cimento (1955-1965) 26 (1962) 1–31, Springer.
[22] U. Frisch, in: A.T. Bharucha-Reid (Ed.), Wave Propagation in Random Media, in: Probabilistic Methods in Applied Mathematics, vol. I, Academic Press Inc., New York, 1970, pp. 75–198.
[23] Joseph A. Turner, Elastic wave propagation and scattering in heterogeneous, anisotropic media: Textured polycrystalline materials, J. Acoust. Soc. Am. 106 (2) (1999) 541–552, Acoustical Society of America.
[24] Xue Bai, Yang Zhao, Jian Ma, Yunxi Liu, Qiwu Wang, Grain-size distribution effects on the attenuation of laser-generated ultrasound in α-titanium alloy, Materials 12 (1) (2018) 102, MDPI.
[25] Saju T Abraham, S Shivaprasad, CR Das, SK Albert, B Venkatraman, Krishnan Balasubramaniam, Effect of grain size distribution on the acoustic nonlinearity parameter, J. Appl. Phys. 127 (18) (2020) AIP Publishing.
[26] Yuan Liu, Michał K. Kalkowski, Ming Huang, Michael J.S. Lowe, Vykintas Samaitis, Vaidotas Cicėnas, Andreas Schumm, Can ultrasound attenuation measurement be used to characterise grain statistics in castings? Ultrasonics 115 (2021) 106441, Elsevier.
[27] Andrea P. Argüelles, Von Kármán spatial correlation function to describe wave propagation in polycrystalline media, J. Appl. Phys. 131 (22) (2022) AIP Publishing.
[28] Wonsup Song, Vikram Krishnaswamy, Raghuram V. Pucha, Computational homogenization in RVE models with material periodic conditions for CNT polymer composites, Compos. Struct. 137 (2016) 9–17, Elsevier.
[29] Eduardo G. Rodriguez, Daniel Millan, Christian Peco, Representative volume element (RVE) analysis for mechanical characterization of ice with metallic inclusion of micro/nano particles, Mec. Comput. 40 (2023) 873.
[30] Kyungmin Baek, Wonseok Lee, Hyunseong Shin, Maenghyo Cho, Multiscale study on determining representative volume elements size for mechanical behaviours of complex polymer nanocomposites with nanoparticulate agglomerations, Compos. Struct. 253 (2020) 112796, Elsevier.
[31] A. El Moumen, T. Kanit, A. Imad, Numerical evaluation of the representative volume element for random composites, Eur. J. Mech. A Solids 86 (2021) 104181, Elsevier.
[32] Eduardo G. Rodriguez, Christian Peco, Daniel Millan, Representative volume element (RVE) analysis for mechanical characterization of ice with metallic inclusion of micro/nano particles, Mec. Comput. 39 (2022) 217.
[33] Martin Ryzy, Tomáš Grabec, Petr Sedlák, István A Veres, Influence of grain morphology on ultrasonic wave attenuation in polycrystalline media with statistically equiaxed grains, J. Acoust. Soc. Am. 143 (1) (2018) 219–229, Acoustical Society of America.
[34] Anton Van Pamel, Gaofeng Sha, Stanislav I Rokhlin, Michael JS Lowe, Finite-element modelling of elastic wave propagation and scattering within heterogeneous media, Proc. R. Soc. Lond. Ser. A Math. Phys. Eng. Sci. 473 (2197) (2017) 20160738, The Royal Society Publishing.
[35] Ming Huang, Peter Huthwaite, Stanislav I Rokhlin, Michael JS Lowe, Finite-element and semi-analytical study of elastic wave propagation in strongly scattering polycrystals, Proc. R. Soc. A 478 (2258) (2022) 20210850, The Royal Society.
[36] Ming Huang, Stanislav I. Rokhlin, Michael JS Lowe, Appraising scattering theories for polycrystals of any symmetry using finite elements, Phil. Trans. R. Soc. A 380 (2231) (2022) 20210382, The Royal Society.
[37] Farshad Ghanbari, Eduardo G. Rodriguez, Daniel Millán, Francesco Simonetti, Andrea P. Argüelles, Christian Peco, Modeling of wave propagation in polycrystalline ice with hierarchical density gradients, Finite Elem. Anal. Des. 217 (2023) 103916, Elsevier.
[38] Bing Tie, A-S Mouronval, V-D Nguyen, Laurent Series, Denis Aubry, A unified variational framework for the space discontinuous Galerkin method for elastic wave propagation in anisotropic and piecewise homogeneous media, Comput. Methods Appl. Mech. Engrg. 338 (2018) 299–332, Elsevier.
[39] Bing Tie, A.-S. Mouronval, Systematic development of upwind numerical fluxes for the space discontinuous Galerkin method applied to elastic wave propagation in anisotropic and heterogeneous media with physical interfaces, Comput. Methods Appl. Mech. Engrg. 372 (2020) 113352, Elsevier.
[40] H. Kamalinia, Bing Tie, Numerical and analytical studies of attenuation coefficient in 2D matrix-inclusion composites with randomly distributed circular inclusions, Wave Motion 123 (2023) 103225, Elsevier.
[41] George Dassios, Ismo V. Lindell, Uniqueness and reconstruction for the anisotropic Helmholtz decomposition, J. Phys. A: Math. Gen. 35 (24) (2002) 5139, IOP Publishing.
[42] Oleg I. Lobkis, Richard L. Weaver, On the emergence of the Green's function in the correlations of a diffuse field, J. Acoust. Soc. Am. 110 (6) (2001) 3011–3017, Acoustical Society of America.
[43] Michel Campillo, Anne Paul, Long-range correlations in the diffuse seismic coda, Science 299 (5606) (2003) 547–549, American Association for the Advancement of Science.
[44] Kees Wapenaar, Evert Slob, Roel Snieder, Unified green's function retrieval by cross correlation, Phys. Rev. Lett. 97 (23) (2006) 234301, APS.
[45] Kees Wapenaar, Evert Slob, Roel Snieder, Andrew Curtis, Tutorial on seismic interferometry: Part 2—Underlying theory and new advances, Geophysics 75 (5) (2010) 75A211–75A227, Society of Exploration Geophysicists.
[46] Kees Wapenaar, Deyan Draganov, Roel Snieder, Xander Campman, Arie Verdel, Tutorial on seismic interferometry: Part 1—Basic principles and applications, Geophysics 75 (5) (2010) 75A195–75A209, Society of Exploration Geophysicists.
[47] Alexander B. Movchan, Leonid I. Slepyan, Band gap green's functions and localized oscillations, Proc. R. Soc. Lond. Ser. A Math. Phys. Eng. Sci. 463 (2086) (2007) 2709–2727, The Royal Society London.
[48] Massimiliano Gei, AB Movchan, Davide Bigoni, Band-gap shift and defect-induced annihilation in prestressed elastic structures, J. Appl. Phys. 105 (6) (2009) AIP Publishing.
[49] Gennady S. Mishuris, Alexander B. Movchan, Leonid I. Slepyan, Waves in elastic bodies with discrete and continuous dynamic microstructure, Phil. Trans. R. Soc. A 378 (2162) (2020) 20190313, The Royal Society Publishing.
[50] Murthy N. Guddati, Bin Yue, Modified integration rules for reducing dispersion error in finite element methods, Comput. Methods Appl. Mech. Engrg. 193 (3) (2004) 275–287.
[51] Bin Yue, Murthy N. Guddati, Dispersion-reducing finite elements for transient acoustics, J. Acoust. Soc. Am. 118 (4) (2005) 2132–2141, Acoustical Society of America.

[52] Jonás D. De Basabe, Mrinal K. Sen, Grid dispersion and stability criteria of some common finite-element methods for acoustic and elastic wave equations, Geophysics 72 (6) (2007) T81–T95, Society of Exploration Geophysicists.
[53] Gunwoo Noh, Seounghyun Ham, Klaus-Jürgen Bathe, Performance of an implicit time integration scheme in the analysis of wave propagations, Comput. Struct. 123 (2013) 93–105, Elsevier.
[54] Z.C. He, Eric Li, G.R. Liu, G.Y. Li, A.G. Cheng, A mass-redistributed finite element method (MR-FEM) for acoustic problems using triangular mesh, J. Comput. Phys. 323 (2016) 149–170, Elsevier.
[55] Gunwoo Noh, Klaus-Jürgen Bathe, The bathe time integration method with controllable spectral radius: The $\rho\infty$ -bathe method, Comput. Struct. 212 (2019) 299–310, Elsevier.
[56] A. Idesman, B. Dey, A new 3-D numerical approach to the solution of PDEs with optimal accuracy on irregular domains and Cartesian meshes, Comput. Methods Appl. Mech. Engrg. 354 (2019) 568–592, Elsevier.
[57] Romain Quey, Loïc Renversade, Optimal polyhedral description of 3D polycrystals: Method and application to statistical and synchrotron X-ray diffraction data, Comput. Methods Appl. Mech. Engrg. 330 (2018) 308–333, Elsevier.
[58] Hans M. Hilber, Thomas JR Hughes, Robert L. Taylor, Improved numerical dissipation for time integration algorithms in structural dynamics, Earthq. Eng. Struct. Dyn. 5 (3) (1977) 283–292, Wiley Online Library.
[59] Eduardo Kausel, Fundamental Solutions in Elastodynamics: a Compendium, Cambridge University Press, 2006.
[60] Thomas JR Hughes, The Finite Element Method: Linear Static and Dynamic Finite Element Analysis, Courier Corporation, 2012.
[61] Najib N. Abboud, Peter M. Pinsky, Finite element dispersion analysis for the three-dimensional second-order scalar wave equation, Int. J. Numer. Methods Eng. 35 (6) (1992) 1183–1218, Wiley.
[62] David J. Benson, Computational methods in Lagrangian and Eulerian hydrocodes, Comput. Methods Appl. Mech. Eng. 99 (2–3) (1992) 235–394, Elsevier.
[63] Lloyd N. Trefethen, Group velocity in finite difference schemes, SIAM Rev. 24 (2) (1982) 113–136, SIAM.
[64] J. Chung, G.M. Hulbert, A time integration algorithm for structural dynamics with improved numerical dissipation: The generalized-α method, J. Appl. Mech. 60 (2) (1993) 371–375, ASME.
[65] Thomas J.R. Hughes, Karl S. Pister, Robert L. Taylor, Implicit-explicit finite elements in nonlinear transient analysis, Comput. Methods Appl. Mech. Engrg. 17–18 (1979) 159–182, Elsevier.
[66] Derek Gaston, Chris Newman, Glen Hansen, Damien Lebrun-Grandié, MOOSE: A parallel computational framework for coupled systems of nonlinear equations, Nucl. Eng. Des. 239 (10) (2009) 1768–1778.
[67] Yingjie Liu, Christian Peco, John Dolbow, A fully coupled mixed finite element method for surfactants spreading on thin liquid films, Comput. Methods Appl. Mech. Engrg. 345 (2019) 429–453, Elsevier.
[68] Joe Sgarrella, Farshad Ghanbari, Christian Peco, I-STL2MOOSE: From STL data to integrated volumetrical meshes for MOOSE, SoftwareX 21 (2023) 101273, Elsevier.
[69] PH Gammon, H. Kiefte, MJ Clouter, WW Denner, Elastic constants of artificial and natural ice samples by brillouin spectroscopy, J. Glaciol. 29 (103) (1983) 433–460, Cambridge University Press.
[70] Chi-Sing Man, Crystallographic texture and group representations, J. Elasticity 149 (1) (2022) 3–445, Springer.